

Life Prediction of Composite Armor in an Unbonded Flexible Pipe

James S. Loverich

Thesis submitted to the Faculty of the Virginia Polytechnic Institute and State
University in partial fulfillment of the requirements for the degree of

Master of Science
in
Engineering Mechanics

Kenneth L. Reifsnider
Michael W. Hyer
Scott L. Hendricks

April 29, 1997
Blacksburg, Virginia

Keywords: Flexible pipe, Offshore, Composites, Elevated temperatures, Fatigue,
Bend-compression rupture, Life prediction

Life Prediction of Composite Armor in an Unbonded Flexible Pipe

James S. Loverich

(ABSTRACT)

Composite materials are under consideration for the replacement of steel helical tendons in unbonded flexible pipes utilized by the offshore oil industry. Higher strength to weight ratios and increased corrosion resistance are the primary advantages of a composite material for this application. The current study focuses on the life prediction of a PPS/AS-4 carbon fiber composite proposed for the above employment. In order to accomplish this task, the properties of the material were experimentally characterized at varying temperatures, aging times and loadings. An analytic technique was developed to predict tensile rupture behavior from bend-compression rupture data. In comparison to tensile rupture tests, bend-compression rupture data collection are uncomplicated and efficient; thus, this technique effectively simplifies and accelerates the material characterization process. The service life model for the flexible pipe composite armor was constructed with MRLife, a well established performance simulation code for material systems developed by the Materials Response Group at Virginia Tech. In order to validate MRLife for the current material, experimental data are compared to life prediction results produced by the code. MRLife was then applied to predict the life of the flexible pipe composite armor in an ocean environment. This analysis takes into account the flexible pipe structure and the environmental and mechanical loading history of an ocean service location. Several parameter studies of a flexible pipe in a hypothetical environment were conducted. These analyses highlight certain loadings and conditions which are particularly detrimental to the life of the material.

Dedication

This work is dedicated to my family: parents, Gene and Donna, brothers, Jeremy, Jacob and Joe and sister, Jean Marie.

Acknowledgments

The author would like to thank the following people for their contributions to this work:

- Dr. Reifsnider for his advice and support over the past two years. He always set aside time to address his students' problems and concerns despite juggling the craziest schedule I have ever seen a person handle.
- Drs. Hyer and Hendricks for being on my graduate committee and teaching two of the most challenging and valuable classes I had at Virginia Tech. I especially want to thank Dr. Hyer for his assistance in my first semester as his teaching assistant.
- Department of Commerce Technology Administration, NIST-ATP program for their financial support.
- Dr. Scott Case for always being there to answer innumerable questions ranging from, "What's wrong with the computers?" to "Can you explain this evolution integral thing?"
- Mac McCord for his technical expertise and experimental wizardry.
- Sheila Collins for keeping all of our schedules, projects and minds running smoothly and in the right direction.
- Blair Russel and Celine Mahieux, my two co-conspirators on the Wellstream Project. Aside from just being a good guy in general, Blair was responsible for collecting almost all of this project's data and essentially ran the whole project.
- The entire Materials Response Group - an entertaining and knowledgeable group of jokers that I was proud to be a part of.

Table of Contents

1. INTRODUCTION.....	1
1.1 OBJECTIVE.....	2
2. LITERATURE REVIEW.....	4
2.1 MATERIAL.....	4
2.1.1 AS-4 Carbon Fibers	4
2.1.2 PPS Resin.....	5
2.1.3 Composites with PPS matrix	5
2.2 MICROMECHANICAL MODELS	7
2.2.1 Tensile Strength Models	7
2.2.2 Compression Strength Models.....	9
2.3 LIFE PREDICTION OF COMPOSITE MATERIALS	9
2.4 STRESS ANALYSIS AND LIFE PREDICTION OF FLEXIBLE PIPES	12
3. EXPERIMENTAL CHARACTERIZATION	15
3.1 MATERIAL.....	15
3.2 QUASI-STATIC TENSION	16
3.3 ROOM TEMPERATURE FATIGUE	17
3.4 ELEVATED TEMPERATURE FATIGUE	18
3.5 BENDING RUPTURE	19
3.5.1 Stress vs. Fixture Length Analysis.....	20
3.5.2 Bend-compression data collection	23
3.6 TENSILE RUPTURE	25
3.7 DYNAMIC MECHANICAL ANALYSIS.....	26
4. PREDICTION OF ELEVATED TEMPERATURE TENSILE RUPTURE BEHAVIOR	28
4.1 ANALYSIS	29
4.1.1 Bending Rupture Model	30
4.1.2 Tensile Rupture Model	35
4.1.3 Predict Tensile Rupture.....	37
4.2 CONCLUSIONS FOR THE TENSILE RUPTURE PREDICTION	43
5. DISCUSSION AND VERIFICATION OF ELEVATED TEMPERATURE LIFE PREDICTION	44
5.1 MRLIFE OVERVIEW [37].....	44
5.2 CODE VALIDATION.....	47
6. COMPOSITE ARMOR LIFE PREDICTION	51
6.1 UNBONDED FLEXIBLE PIPE STRESS ANALYSIS	51
6.1.1 Cylindrical layer stiffness.....	53
6.1.2 Helical layer stiffness	54
6.1.3 Total pipe stiffness.....	55
6.1.4 Stresses due to pipe bending	56
6.2 IMPLEMENTATION OF LOADING HISTORY INTO THE LIFE PREDICTION CODE.....	57
6.3 PARAMETER ANALYSIS OF A HYPOTHETICAL FLEXIBLE PIPE	61
6.3.1 Pipe description and loading	61
6.3.2 Conclusions drawn from the hypothetical pipe analysis	63
7. CONCLUSIONS AND FUTURE WORK	65
7.1 FUTURE WORK	65
8. REFERENCES.....	67

9. APPENDIX A - HYPOTHETICAL UNBONDED FLEXIBLE PIPE ANALYSIS.....	72
10. APPENDIX B - ITERATIVE REMAINING STRENGTH CALCULATION PROGRAM.....	80
11. VITA	84

List of Figures

Figure 1.1 Flexible pipe service environment and structure	1
Figure 3.1 Specimen geometry for room temperature tensile tests	16
Figure 3.2 Room temperature fatigue test data. $R = 0.1$, $f = 10$ Hz	18
Figure 3.3 Elevated temperature (90°C) fatigue data. $R = 0.1$, $f = 10$ Hz.....	18
Figure 3.4 Bend-compression rupture fixture. Pictured from top down: adjustable fixture, fixture with loaded specimen, and high capacity long-term fixture	19
Figure 3.5 Compression bending loading condition.	21
Figure 3.6 Normalized strain vs. fixture length.....	22
Figure 3.7 Bend-compression rupture failure criterion	23
Figure 3.8 Bend-compression rupture data at 90°C	24
Figure 3.9 Comparison of dry and salt water bend-compression rupture tests at 90°C ...	24
Figure 3.10 Tensile rupture specimen	25
Figure 3.11 Tensile rupture data at 90°C	26
Figure 3.12 Dynamic Mechanical Analysis of Baycomp material	27
Figure 4.1 Assumed shape of local buckling in a composite in compression. Initial state (left) and deformed state (right)	31
Figure 4.2 Free body diagram of the representative volume element used in the compression model.....	31
Figure 4.3 Geometry of initial fiber misalignment used to simplify the compression strength model	34
Figure 4.4 Arrangement of fiber breaks in the vicinity of a matrix crack	36
Figure 4.5 Shear strength of PPS matrix vs. Temperature	39
Figure 4.6 Modulus of PPS matrix vs. Temperature.....	40
Figure 4.7 Bend-compression rupture data at 90°C and curve fit.....	41
Figure 4.8 Comparison of tensile rupture curve prediction and tensile rupture data	42
Figure 5.1 The use of remaining strength as a damage metric	45
Figure 5.2 Tensile rupture curve fit and data	48
Figure 5.3 Room temperature fatigue fit and S-N curve fit	49
Figure 5.4 Comparison of elevated temperature fatigue prediction and 90°C fatigue data	50
Figure 6.1 Structure of an unbonded flexible pipe with composite tensile strength (armor) layers.....	52
Figure 6.2 Stresses and loads on a cylindrical layer.....	53
Figure 6.3 Helical layer geometry and applied forces	54
Figure 6.4 Maximum and minimum stress boundaries for a hypothetical pipe loading due to the wave scatter diagram in Table 6.3.....	58
Figure 6.5 Approximated helical armor stress with respect to time.....	59
Figure 6.6 Remaining strength vs. time for composite armor.....	63

List of Tables

Table 3.1 Quasi static tension test data	16
Table 3.2 Quasi static tension test data of aged specimens.....	17
Table 4.1 Properties of AS-4 carbon fiber	39
Table 4.2 Slope ratio (Rs) at different temperatures	40
Table 6.3 Simplified wave scatter diagram for a 48 hour time period.....	58
Table 6.4 Normalized armor stress, wave period and time interval length for each load case	62

1. Introduction

Recent advances in the performance and reduced cost of composite materials have made them feasible for previously unexplored applications. One such application is unbonded flexible pipe utilized by the extremely competitive offshore oil industry where increased well head depths and cost effectiveness are placed at a premium.

Flexible pipes are used as dynamic risers to connect floating production facilities to seabed flowlines. Figure 1.1 demonstrates the employment of a flexible pipe as a

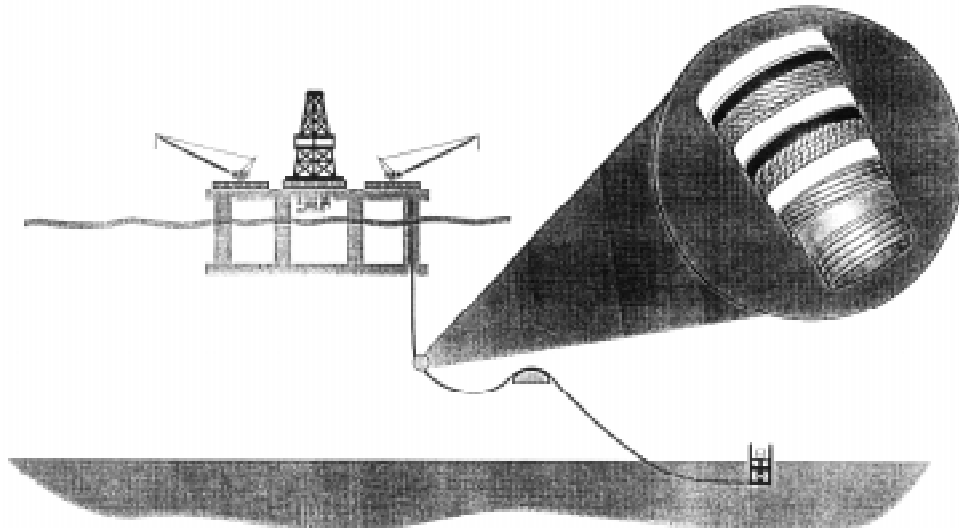


Figure 1.1 Flexible pipe service environment and structure

dynamic riser and displays the structure of a typical flexible pipe. Flexible pipes are also used in situations where their installation is more cost effective than rigid pipe or where recovery for reuse is necessary. The achievement of greater well head depths requires a reduction in the pipe weight; the extreme depths projected for these pipes can actually cause them to rupture under their own weight. Light weight pipes may also be valuable as static flowlines deployed in arctic environments.

In order to reduce the weight of flexible pipes, replacement of standard steel armor tendons with composite materials is being considered. A weight reduction of 30% is expected for a composite pipe designed to the specifications of a comparable conventional flexible pipe. In addition to lighter weight, composite materials offer higher strength and increased corrosion resistance.

Wellstream Inc. is introducing composites into some of their deep water flexible pipes. They are considering a unidirectional pultruded Polyphenylene Sulfide (PPS) / AS-4 carbon fiber composite tape manufactured by Baycomp as a replacement for helically wound steel tendons.

1.1 Objective

The focus of the current study is the characterization and life prediction of the Baycomp material for its intended application as helical armor tendons in a flexible pipe. Characterization is to include the effects of fatigue, elevated temperatures up to 90°C and environmental degradation due to seawater. Aging and long-term mechanical performance of the material will also be studied.

One sub-objective of this research was to develop an analytical model to determine tensile rupture behavior from bend-compression rupture data. Long-term tensile rupture behavior under aggressive environments is a significant failure mechanism of this material and; therefore, must be characterized. Tensile rupture experiments are time consuming and become complex with the introduction of elevated temperature and/or a corrosive environment. Bend-compression rupture tests, on the other hand,

utilize an uncomplicated fixture and can accommodate large numbers of specimens in a wide variety of environments. The application of this model, which is based on several micromechanics concepts, “accelerates” the material characterization process and may be applicable to other material systems.

The service life model for the flexible pipe is constructed with MRLife, a performance simulation code for material systems developed by the Materials Response Group at Virginia Tech [1]. This program uses experimental data and analytical tools to predict the long-term behavior of a composite. Several modifications to the code are implemented to better represent the loading and material under study. The code is verified for the PPS/AS-4 carbon fiber material via comparison of experimental data to the predicted life. Finally, the life of composite armor tendons within a flexible pipe is investigated. The life prediction model considers a pipe stress analysis and the expected loading history of the pipe in an ocean environment.

2. Literature Review

The objective of this review is to establish the literature base which encompasses the following topics: characterization of the material under study, micromechanical modeling of composite strength, life prediction for composite materials and the analysis of unbonded flexible pipes.

2.1 Material

This section presents information pertaining to the properties of the Polyphenylene Sulfide (PPS) / AS-4 carbon fiber composite under study and its constituent materials. Literature discussing other composite systems which have a PPS matrix are also included since conclusions can be drawn regarding the performance of PPS as a matrix in aggressive environments.

2.1.1 AS-4 Carbon Fibers

Wimolkiatisak and Bell [2] investigated coatings on Hercules AS-4 carbon fibers which improve the interfacial shear strength and toughness of a composite. Single fiber fracture tests at various temperatures were conducted to determine these properties. Of particular significance to the current study are the data obtained for fiber fracture strength as a function of gauge length. Weibull distribution parameters for AS-4 fibers extracted from this data are employed in the micromechanics model in Section 4.1.2.

2.1.2 PPS Resin

Ma [3] presented the rheological, thermal and morphological properties of several high performance thermoplastic resins including PPS. The dynamic viscosity, storage modulus and loss modulus were established at various temperatures. This publication describes the effect of adding carbon fiber to the resin on thermal stability and environmental performance. Also noted are the morphological properties of thermally aged PPS. Conclusions on the effect of crosslinking and chain-extension reaction were reached.

Schwartz and Goodman[4], Brydson [5] and Harper [6] presented information regarding the material properties of neat PPS resin. These sources provided strength and stiffness values as functions of temperature, melting and glass transition temperatures and molecular structure diagrams. Also discussed were the notable properties of PPS which include: heat resistance, flame resistance, chemical resistance, and electrical insulation.

2.1.3 Composites with PPS matrix

Yau et. al. [7] presented the properties of improved PPS/E-Glass and PPS/AS-4 carbon fiber composites. The new PPS polymer is characterized by high toughness and adheres well to both carbon and glass fibers. Composite properties under hot/wet environmental conditions are enhanced by choosing appropriate material sizings. Mechanical properties at high temperatures (93-115°C) were retained to a level of at least 80%. Durability and mechanical property data were discussed as well as processing options and ongoing characterization efforts.

Myers [8] performed a variety of tests to determine the viscoelastic properties of PPS/carbon fiber composites. These tests included: three and four point flexure, centrosymmetric disk (CSD) and torsion. The material considered was constructed with a quasi-isotropic layup of carbon fiber fabric. Testing showed that “fiber-dominated” modes (flexure loading) have a smaller loss in stiffness than the “resin-dominated” modes (torsion and CSD). Projections for the ten-year modulus were produced from the tests and imply that the viscoelastic response is stress state dependent - a “resin-dominated” mode will experience greater change.

Lou and Murtha [9] reported results of linear and nonlinear 1,000 hour creep tests for glass fiber/PPS stampable composites. The swirl pattern of the reinforcing fibers caused the composite to have a strong viscoelastic component. The test temperatures were incremented from 24 to 177°C. One curious observation was that the measured creep at 177°C was actually less than at 24°C. This phenomenon is possibly due to composite shrinkage produced by the release of residual stresses or by microstructural changes. Creep of neat PPS resin was also studied.

Ma et. al. [10] investigated the effect of physical aging on the penetration impact toughness and Mode I interlaminar fracture toughness of PPS/carbon fiber and PEEK/carbon fiber composites. The materials studied were aged below their glass transition temperature for varying periods of time. They concluded that aging has a noticeable effect on the composite toughness. In general, it was observed that the toughness decreased with an increase in aging temperature and time period. It should be noted that the properties initially decreased relatively quickly with respect to time, but then appeared to reach a lower limit of around 85% of their original value.

Ma et. al. [11] also conducted a study of the effect of physical aging on the mechanical properties of PPS/carbon fiber and PEEK/carbon fiber composites. Included in this publication was a discussion of enthalpy-relaxation through physical aging determined by DSC analysis. The loss modulus and loss tangent were observed during the relaxation process. The tensile and flexural strengths of the PPS composite were determined at various aging temperatures and time periods. Both glass transition temperatures and mechanical properties of the composites actually increased with aging time.

2.2 Micromechanical Models

In the following section, several of the more prominent micromechanical models for strength will be outlined. First, tensile strength models will be discussed, followed by compressive strength models.

2.2.1 Tensile Strength Models

The most simple approximation for the strength of a unidirectional composite is the rule-of-mixtures approach suggested by Kelly and Nicholson [12]. For this model the composite strength is written as:

$$X_t = X_f V_f + X_m (1 - V_f) \quad (2.1)$$

where X_t is the composite strength, X_f and X_m are the tensile strengths of the fiber and matrix respectively, and V_f is the fiber volume fraction. It should be noted that this one-

dimensional model does not consider fiber - matrix interaction or the statistical distribution of defects within each constituent.

Batdorf [13] developed a probability analysis to predict tensile strength of polymer matrix composites. He considered a composite in which damage is manifested only as fiber breakage. As fibers fracture, stress concentrations are produced which act over an ineffective length. Failure occurs when these stress concentrations lead to multiple fiber breaks and (eventually) instability. In order to determine the ineffective length and stress concentrations on the unbroken fibers, Gao and Reifsnider [14] developed a model based on shear-lag assumptions. Their model consists of a central core of broken fibers surrounded by: matrix, then unbroken fibers, and finally a homogeneous effective material. Equilibrium equations are written for this model and then solved to find the ineffective length and stress concentrations.

Reifsnider et. al. [15] suggested a model similar to Batdorf's above, but they define the failure criterion differently. They assume that failure occurs when the number of fiber groups with $n+1$ adjacent fiber breaks is equal to the number of fiber groups with n adjacent fiber breaks multiplied by the number of fibers surrounding the n adjacent fiber breaks, for all n .

Curtin [16] presented a model to predict uniaxial tensile strength for ceramic matrix composites. He assumes that each fiber fractures independently and that the load it originally supported is distributed globally among the remaining intact fibers. This process can be modeled as a single fiber in a homogeneous matrix. Based on these assumptions the tensile strength is derived as a function of: the statistical fiber strength,

fiber radius, fiber volume fraction and interfacial shear strength. Good agreement between these predictions and data from the literature was reported.

2.2.2 Compression Strength Models

Tsai and Hahn [17] presented a micromechanics model for uniaxial compression. They considered a representative volume element with a given initial fiber misalignment. Equilibrium equations for the representative volume element can be written and solved to determine the compressive stress as a function of the fiber misalignment and the composite effective shear modulus. Failure is defined as the point at which the maximum local shear stress reaches the shear strength of the composite.

Budiansky and Fleck [18] approached the compression strength problem by studying a microbuckled (kink band) region within a unidirectional composite. This kink band has an initial misalignment angle, ϕ_0 , and an inclination angle, β . The material in the kink band is assumed to be homogeneous but anisotropic. The compressive strength is derived based on the behavior of the kink band as an elastic region, rigid-perfectly plastic region or elastic-perfectly plastic region. They also include an analysis for the propagation of the microbuckled zone into undamaged material.

2.3 Life Prediction of Composite Materials

Reifsnider et. al. [19] have developed a concept and methodology to represent durability and damage tolerance in composite materials. The strength and life of a composite material are assumed to be reduced by damage accumulation. Damage

accumulation consists of the various damage and failure modes that act and interact to progressively degrade a composite material. A derivation for the strength evolution equation which is used to predict remaining strength from damage accumulation was provided. Also introduced were several additions to the evolution equation that increase its utility. Of special interest to this research is a concept which combines the effects of time and cycle dependent damage modes. Implementation of the evolution equation is accomplished via a computer code known as MRLife.

Reifsnider et. al. [20] again discussed the damage accumulation scheme described in the paragraph above. In this paper more emphasis was placed on the implementation of the MRLife code. The methods and equations used to model strength and stiffness reductions in the evolution equation were presented. Several hypothetical MRLife runs were studied. These runs considered: ply-level strength changes due to environmental attack and viscoelastic creep, matrix degradation and ply-level stiffness changes. In addition to life prediction, MRLife can be employed to optimally “design” composite material systems for longevity. MRLife results have been compared with experimental data in this paper and in numerous other sources [1]. All of which conclude that MRLife is an effective predictive tool, applicable to most composite material systems.

Argon and Bailey [21] conducted monotonic and cyclic tension experiments of transparent laminates. The nature of the composite allowed them to study the mode by which the specimens failed and the intermediate stages of damage. The tensile stress distribution in monotonic loading correlated well with a statistical theory. The fatigue tests were effected by matrix damage caused by humidity. The same damage was so also present in static loading “control group”, therefore no conclusions could be reached

regarding the fatigue failure mode. They also noted that elements of composite materials can be damaged in the lamination process and that this should be taken into account in quantitative analyses.

Kliman et. al. [22] investigated the life prediction of materials under varied loading histories. For a given service-loading over time, a probability concept for predicting the fatigue lifetime was developed. The analysis calculates a distribution function of the residual fatigue lifetime for a given loading regime. Both the loading history and the random nature of the material is taken into account by this distribution. The predictions showed good agreement with experimental results.

Shah [23] suggested a probabilistic model for fatigue lifetime prediction in polymeric matrix composite materials. The analysis takes into account matrix degradation due to cyclic thermal and mechanical loads. Uncertainties in the various composite constituent properties are included in the model. A $(0/\pm 45/90)_s$ laminate was studied at low and then high thermal and mechanical loads. The results showed that at lower loadings the composite life is most sensitive to matrix compressive strength, matrix modulus, thermal expansion coefficients and ply thickness. At higher loadings the life is most sensitive to matrix shear strength, fiber longitudinal modulus, matrix modulus and ply thickness.

Jacobs et. al. [24] studied the effect of fretting fatigue on composite laminates. Experimental data were obtained by pressing two metal pins against the sides of the specimen while a fatigue test was in progress. The pin contact pressure, laminate lay-up and slip amplitude were varied. Results of the investigation showed that fretting could substantially reduce the fatigue life of a composite material, especially when the load

bearing 0° layers are damaged. Consideration of the damage mechanisms of fretting allowed them to develop a quantitative method for fretting fatigue prediction.

2.4 Stress Analysis and Life Prediction of Flexible Pipes

Claydon et. al. [25] presented a service life prediction method for an unbonded flexible pipe under cyclic loading conditions. An in-house software package was developed which is capable of predicting the service life for any particular pipe layer at a given pipe axial and circumferential location. Life prediction is based on the combination of a wear model that depends on interlayer pressures and slip distances and a mechanical fatigue model that takes into account the stress increase due to wear-induced cross-sectional area losses. Also included is an overview of the flexible pipe stress analysis implemented in their software package.

Saevik and Berge [26] developed a model for analyzing the stresses and slip in armor tendons of nonbonded flexible pipes. They used an eight degree of freedom, curved beam finite element model which took into account arbitrary curvature distributions along the pipe, end restraints and friction effects. Two nonbonded 4-inch internal diameter flexible pipe specimens were studied to verify the analysis results. The pipes were exposed to dynamic loading conditions until fatigue failure occurred in the tensile armor layers. The failure modes were identified as pure fatigue of both layers in one specimen and fretting fatigue of the inner layer for the other specimen. Good correlation was found between the observed and theoretical fatigue behavior.

Neffgen [27] developed a management system (LAMS) which uses analytical software and reliability criteria to determine service life. The program takes into account: gas-permeation, effects of corrosive agents, aging, cathodic potential, and reductions in cross-section of the helical armor due to fretting fatigue. LAMS can be utilized to formulate maintenance plans, training programs, and an overall operational strategy.

Ismail et. al. [28] presented a description of the design process for flexible risers. Selection criteria for riser configurations in deep and shallow water were compared to riser dynamic analyses conducted with a computer numeric model. The model generates time histories of the forces and wave surface profiles in addition to the expected range of the axial force and riser coordinates. They concluded that motion produced by the combined flow of waves, currents and vessel heave motion is significant in the design of riser configuration.

Kalman et. al. [29] described the implementation of advanced materials in flexible pipe construction. Among the new materials considered are composite helical armor tendons. The high strength to weight ratio of composites relative to steel leads to a lighter weight pipe; thus, reducing top tension and deck loads on production facilities and extending the maximum allowable free-hanging depth of the pipe. The results of tests conducted to verify the strength of the composite material under study and its resistance to fatigue and abrasion were presented.

Robinson et. al. [30] described the constituents, installation and quality control of flexible pipe. A detailed description of each layer in a flexible pipe was provided including: material, geometry, strength, environment, manufacturing process, and design codes. Of particular interest to this research was the discussion of the tensile tendons

which are installed in a helical manner with a lay angle of 30 to 55 degrees with respect to the longitudinal axis. Also discussed was the pipe installation process and possible pipe service configurations.

3. Experimental Characterization

In order to characterize the material under study, a wide range of experiments were conducted. Included in these tests were: quasi-static tension at room and elevated temperatures of aged and unaged material, fatigue tests at room and elevated temperatures, tensile rupture tests at elevated temperature, end-loaded bend-compression rupture tests at elevated temperature, and a dynamic-mechanical analysis.

3.1 Material

The material, supplied by Baycomp, is a PolyPhenylene Sulfide matrix / AS-4 carbon fiber composite. Specimens were produced from the unidirectional pultruded tape with a 0.5" x 0.04" cross-section. Six-inch long specimens were used for all tests, except the elevated temperature tests and dynamic-mechanical analysis. In order to accommodate the use of a furnace, eight-inch long specimens were used for the elevated temperature tests. A diamond saw was used to cut the tape to the required lengths. Glass/epoxy end tabs were applied to the specimen ends for quasi-static tension, tensile rupture and fatigue tests in order to prevent specimen damage in the grip area. The ends of the specimen and the tabbing material were grit blasted to improve the adhesion of the bonding epoxy. It was not necessary to tab the specimens used for the end-loaded bending rupture tests. The six-inch test specimen geometry is shown in Figure 3.1.

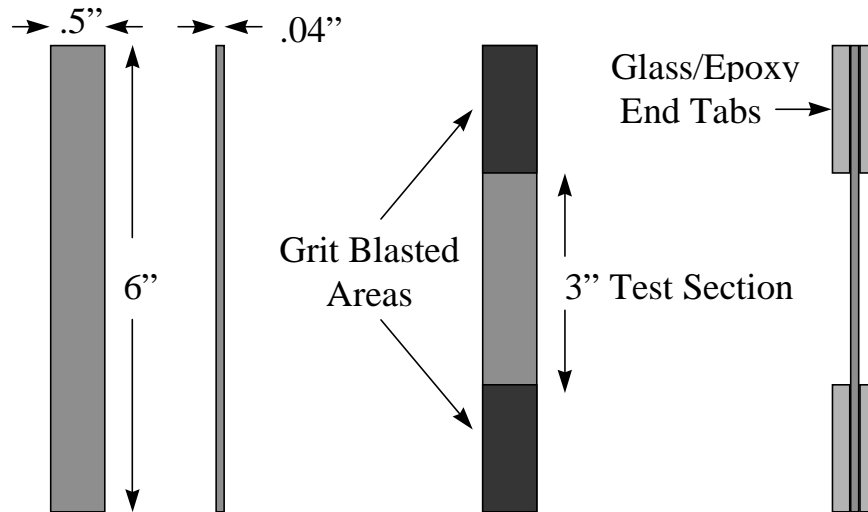


Figure 3.1 Specimen geometry for room temperature tensile tests

3.2 Quasi-static Tension

In order to develop an understanding of the effects of elevated temperatures and aging, quasi-static tension tests were conducted at several temperatures and aging periods. Tension tests of unaged specimens were conducted at 23°C, 90°C and 120°C. The effect of unstressed exposure to elevated temperatures was determined through tests of specimens aged in air at 90°C and 120 °C for 1, 10, 30, and 100 days. Table 3.1 and Table 3.2 summarize the results of these tests.

Table 3.1 Quasi static tension test data

Test Conditions	Modulus Msi	Strength Ksi	Strain to Failure %
23 °C (10 replicates)	14.3 ± .13	186 ± 5.5	1.41 ± .033
90 °C (5 replicates)	13.6 ± .26	188 ± 8.4	1.46 ± .061
120 °C (5 replicates)	13.2 ± .36	174 ± 7.8	1.37 ± .081

Table 3.2 Quasi static tension test data of aged specimens

Test Conditions	Modulus Msi	Strength Ksi	Strain to Failure %
1 Day @ 90 °C (10 replicates)	14.3 ± .44	197 ± 14.4	1.41 ± .13
10 Day @ 90 °C (10 replicates)	14.2 ± .33	199 ± 8.4	1.44 ± .054
30 Day @ 90 °C (10 replicates)	14.2 ± .20	194 ± 6.7	1.46 ± .072
100 Day @ 90 °C (4 replicates)	14.3 ± .70	194 ± 11.6	1.41 ± .061
1 Day @ 120 °C (10 replicates)	14.3 ± .27	209 ± 6.3	1.55 ± .042
10 Day @ 120 °C (10 replicates)	14.0 ± .48	199 ± 12.4	1.50 ± .062
30 Day @ 120 °C (10 replicates)	14.4 ± .26	202 ± 5.4	1.47 ± .053
100 Day @ 120 °C (10 replicates)	14.5 ± .66	194 ± 5.1	1.44 ± .096

Table 3.2 shows that unstressed aging of specimens in air at temperatures as high as 120°C actually enhances the quasi-static tensile behavior and that tests at elevated temperatures produce little change in the strength of the material. Aging of the material did not produce a noticeable change in the stiffness. However, the stiffness decreased slightly with increasing test temperature. The values for the unaged tensile strength are used to normalize stresses in subsequent sections.

3.3 Room Temperature Fatigue

Room temperature fatigue tests were performed at a frequency of 10 Hz with an R-ratio ($\sigma_{\min}/\sigma_{\max}$) of 0.1. Figure 3.2 shows the data gathered in these tests and indicates a relatively flat normalized stress vs. life relationship.

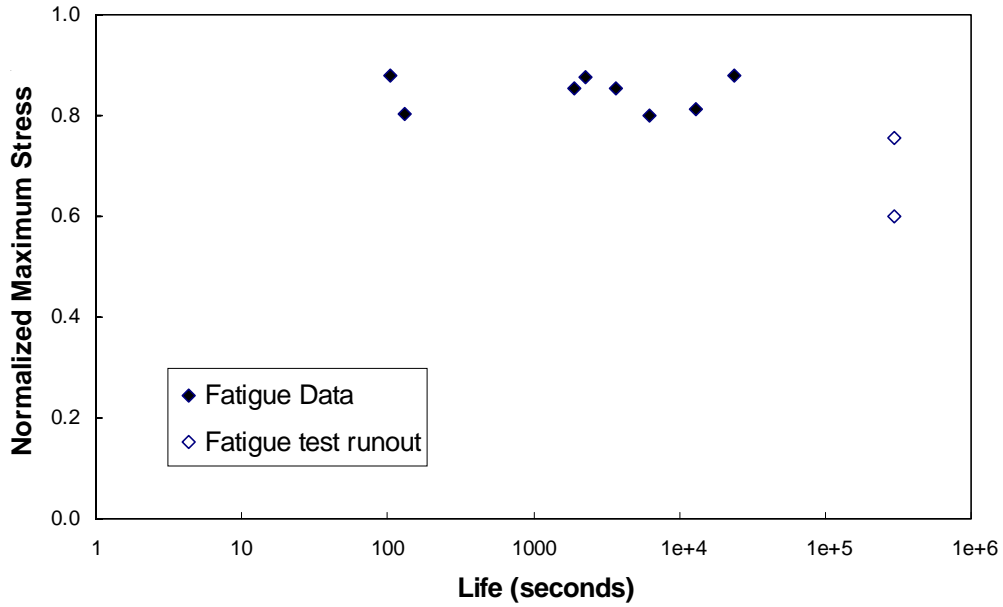


Figure 3.2 Room temperature fatigue test data. $R = 0.1$, $f = 10$ Hz

3.4 Elevated Temperature Fatigue

Fatigue tests at 90°C were conducted in order to verify the elevated temperature life prediction discussed in detail in Chapter 5. These tests were conducted at a frequency

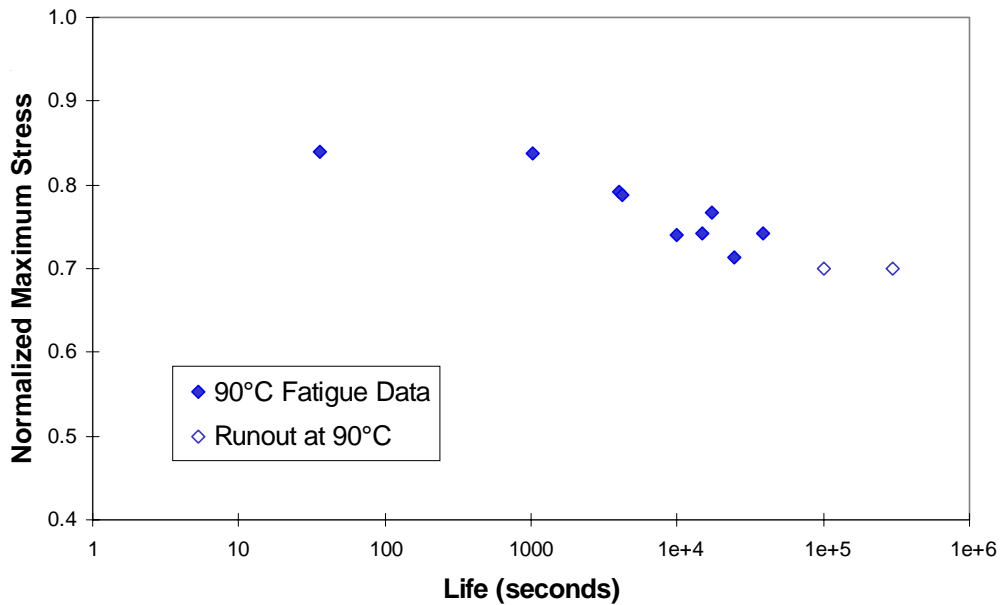


Figure 3.3 Elevated temperature (90°C) fatigue data. $R = 0.1$, $f = 10$ Hz

of 10 Hz with an R-ratio of 0.1. It can be observed by comparing the data in Figure 3.2 and Figure 3.3 that elevated temperature does reduce the material's fatigue life.

3.5 Bending Rupture

Rupture effects at elevated temperatures were studied with an end-loaded bend-compression fixture. This configuration was chosen after experimenting with several types of loading. One of the desired characteristics of this loading is that the matrix contributes directly to the behavior of the composite system. The fixture is also uncomplicated and can accommodate a large number of specimens in a wide variety of environments. The compression bending loading condition requires that only a single axial force be applied on the specimen ends. A large range of strains is obtainable by adjusting the length between the loaded ends of the specimen. Figure 3.4 shows the

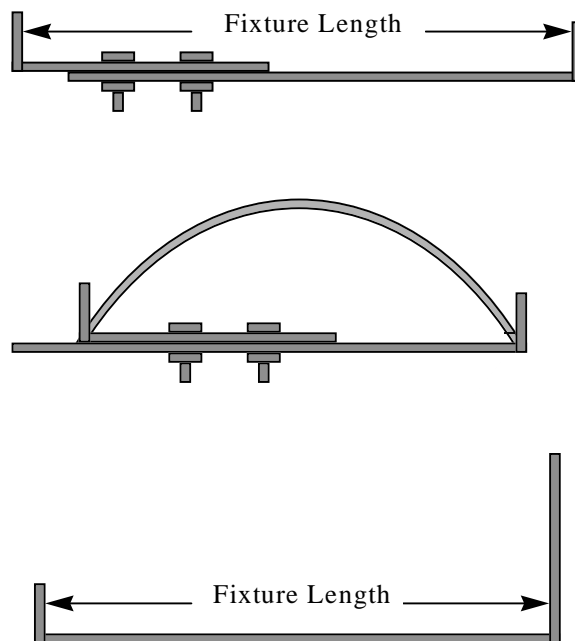


Figure 3.4 Bend-compression rupture fixture. Pictured from top down: adjustable fixture, fixture with loaded specimen, and high capacity long-term fixture

bend-compression fixture in its unloaded and loaded states. Also shown in Figure 3.4 is a fixed-length fixture capable of loading as many as 15 specimens at an equal strain level for long-term testing.

3.5.1 Stress vs. Fixture Length Analysis

In order to determine the required fixture length for a desired maximum stress in the bend-compression rupture specimen, an analysis from Timoshenko and Gere [31] and Fukuda [32,33] in conjunction with classical strength of materials methods was applied. We will now discuss this analysis as presented in [34].

The compression-bending condition is achieved with pinned-pinned end conditions and an applied axial compressive load. One half of the specimen under load is shown in Figure 3.5. Applying the elastic solution from Timoshenko and Gere [31] we can write

$$\frac{\lambda}{L} = 2 - 2 \frac{E(p)}{K(p)} \quad (3.1)$$

$$\frac{\rho}{L} = \frac{1}{2pK(p)} \quad (3.2)$$

where λ is the end deflection, ρ is the radius of curvature, L is one half of the initial specimen length, and $K(p)$ and $E(p)$ are the first and second perfect elliptical integrals as defined in Equation (3.3) and Equation (3.4), respectively.

$$K(p) = \int_0^{\frac{\pi}{2}} \frac{1}{\sqrt{1 - p^2 \sin^2 \phi}} d\phi \quad (3.3)$$

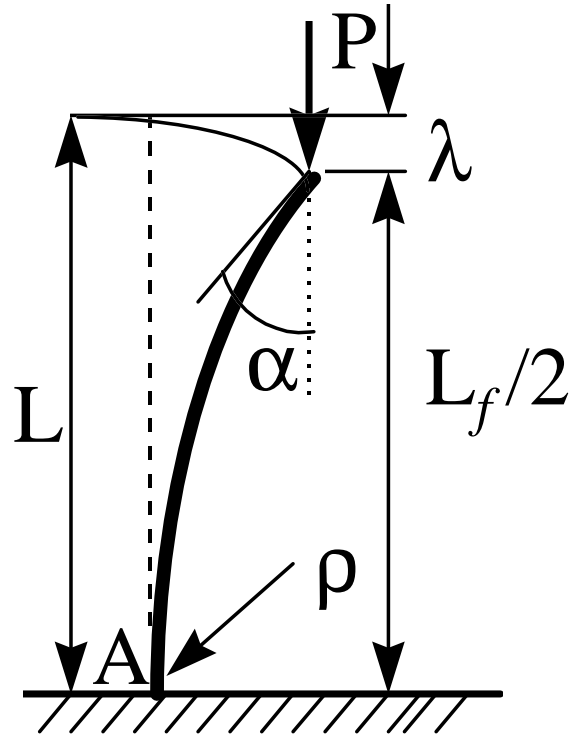


Figure 3.5 Compression bending loading condition.

$$E(p) = \int_0^{\frac{\pi}{2}} \sqrt{1 - (p^2 \sin^2 \phi)} d\phi \quad (3.4)$$

where

$$p = \sin \frac{\alpha}{2} \quad (3.5)$$

The maximum surface strain, ϵ_m , for a given end rotation, α , and specimen thickness, t , is then written as

$$\epsilon_m = \frac{t}{2 \frac{\rho(\alpha)}{L} L} \quad (3.6)$$

Equation (3.6) relates the surface strain (which in turn can be related to stress) to the radius of curvature at the mid-span. Figure 3.6 displays fixture length, in this case $L_f = 2(L-\lambda)$, as a function normalized strain (ϵ/ϵ_0), where ϵ_0 is the failure strain in bending at

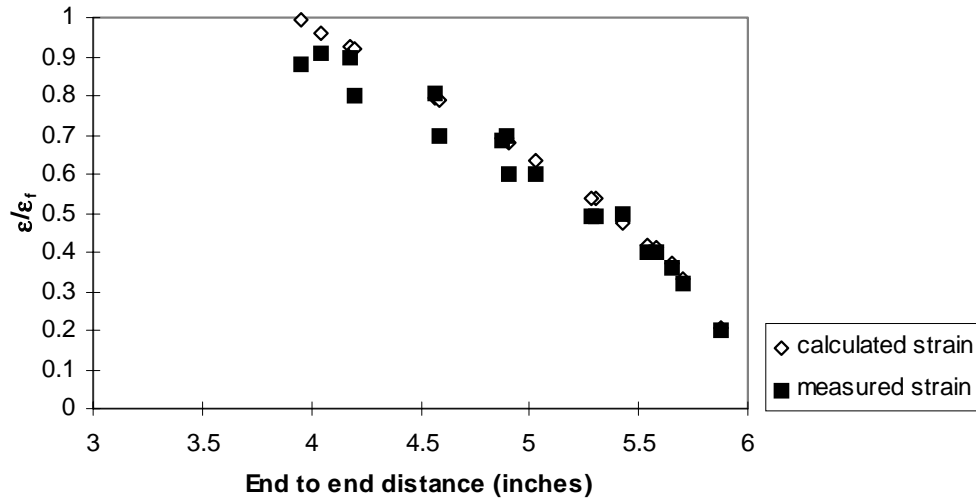


Figure 3.6 Normalized strain vs. fixture length

room temperature. Also included in Figure 3.6 for comparison are the experimental data obtained from strain gages located at the mid-span of specimens loaded in the adjustable fixture.

The calculated values and measured data match quite well; the average error is about 6%. The calculated strains appear to be an upper bound of the measured values. A possible explanation for the error is the fact that the strain gages average the strain around the point of maximum strain and therefore do not report the actual point-wise maximum strain. Another factor which may contribute to the error is that the previous analysis assumed a constant and uniform bending modulus. In reality the compressive and tensile bending moduli may differ slightly so that the zero strain at the mid-plane assumption is no longer exact. Over one hundred specimens have been tested to date which show that there is very little error compared to theoretical expectations and that the data are accurately reproducible.

3.5.2 Bend-compression data collection

The specimen is introduced to aggressive environments simply by placing the entire loaded fixture in an oven or bath containing the desired environment. For this study the specimens were tested in an oven at 90°C. 90°C was chosen since it is the upper design limit for the material under study. Data were also gathered from tests conducted in salt water at 90°C to determine the effects of an ocean environment on the material. Time to failure is defined as the elapsed time between introduction into the oven and failure. Since the material fails initially on the compressive microbuckling side of the specimen, there is not a sudden distinctive failure characterized by fracture into two pieces. The failure criterion is defined as the point in time at which the entire width of the specimen forms a sharp cusp at the failure location. A visual explanation of this failure criterion is displayed in Figure 3.7.

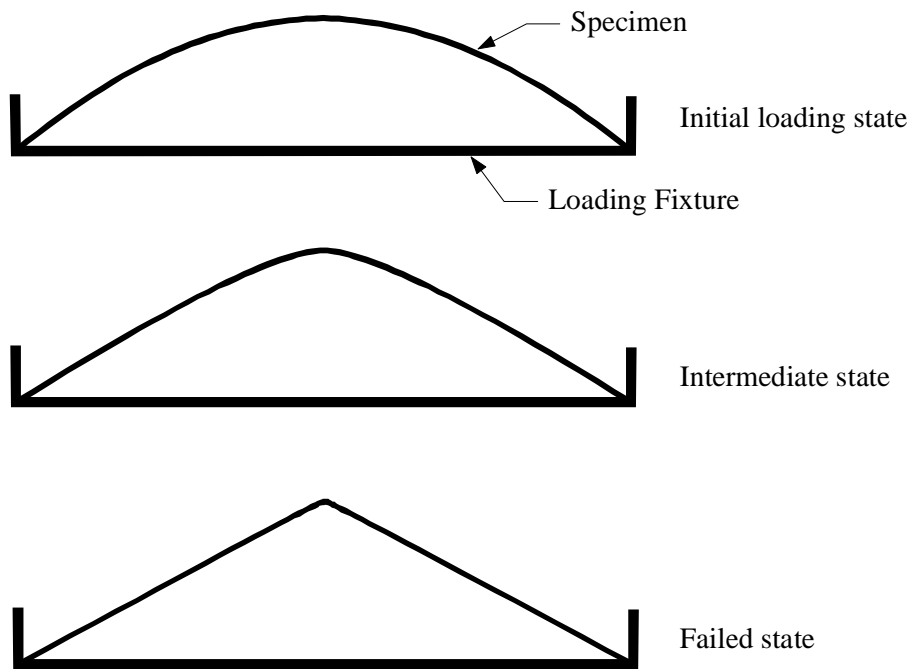


Figure 3.7 Bend-compression rupture failure criterion

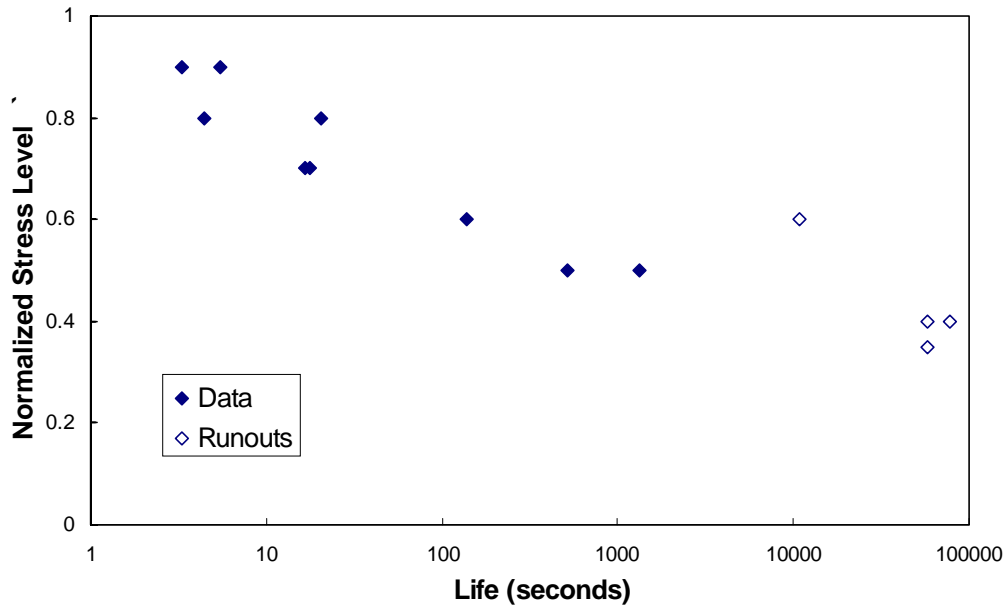


Figure 3.8 Bend-compression rupture data at 90°C

The bend-compression data collected at 90°C are shown in Figure 3.8. As expected, the test durations were fairly short at high strain levels and, below a normalized strain value of 0.60, became significantly longer. When plotted on a semi-log axis, the shape of the data appears to be nearly linear. Figure 3.9 shows the bend compression

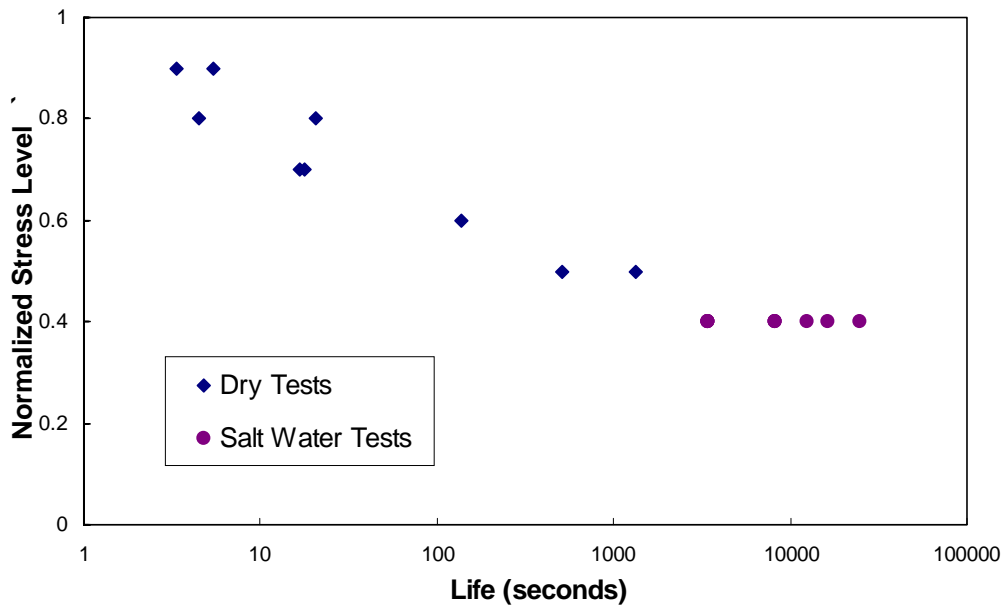


Figure 3.9 Comparison of dry and salt water bend-compression rupture tests at 90°C

rupture data for the salt water tests at 90°C [35] in relation to the dry tests at 90°C. We can conclude from observation of Figure 3.9 that salt water has very little effect on the behavior of the material. This is in good agreement with data obtained from other sources [7].

3.6 Tensile Rupture

Tensile rupture tests were conducted in order to verify the prediction of a tensile rupture curve obtained through via an analytic method (discussed in Chapter 4) which uses bend-compression data as input. Figure 3.10 shows the tensile rupture specimens which were tabbed with 0.125 inch thick glass/epoxy strips to avoid stress concentrations

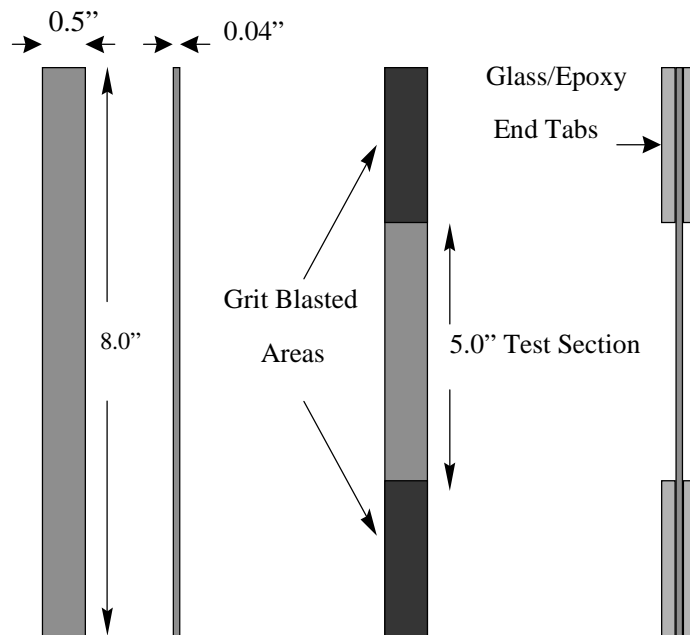


Figure 3.10 Tensile rupture specimen

at the grips. The 8-inch specimens were tested in a constant-load creep frame with elevated temperature capability. 90°C was again used as the evaluation temperature.

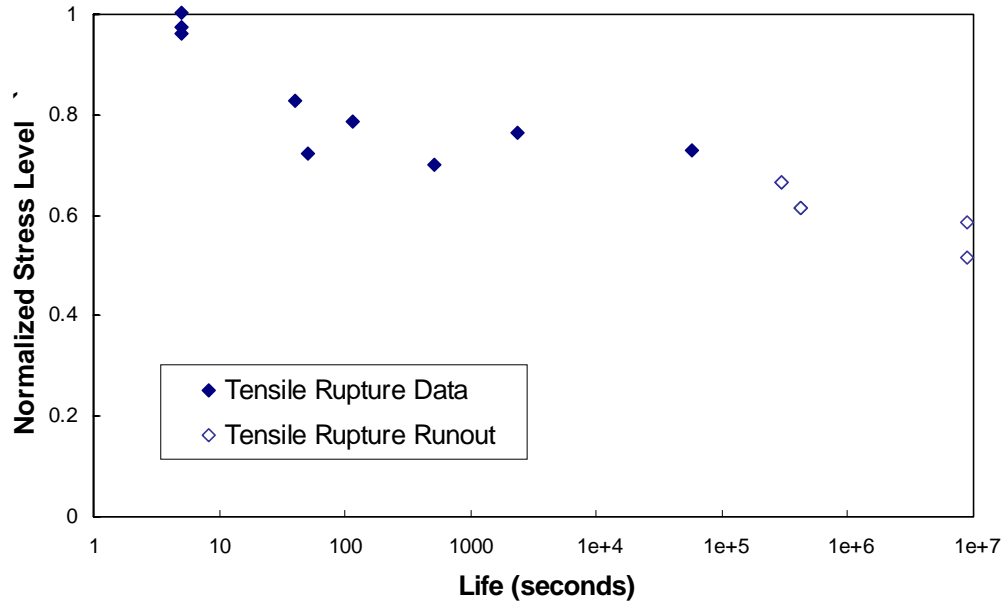


Figure 3.11 Tensile rupture data at 90°C

Time to failure is defined as the elapsed time between application of the load and failure. The failure criterion is the complete separation of the two ends. Data collected from the tensile rupture tests are shown in Figure 3.10. It should be noted that the time periods for tensile rupture failure were considerably larger than the bend-compression rupture times for the same normalized applied stress.

3.7 Dynamic Mechanical Analysis

The glass transition temperature (T_g) of the material was determined by Dynamic Mechanical Analysis (DMA). The DMA was conducted at a fixed frequency of 1 Hz and the temperature was swept from 35°C to 175°C at a rate of 1°C/min. The DMA specimen had dimensions of 1" x 0.5" x 0.04". Figure 3.12 presents the results of the DMA test and shows that the storage modulus begins to relax around 100°C.

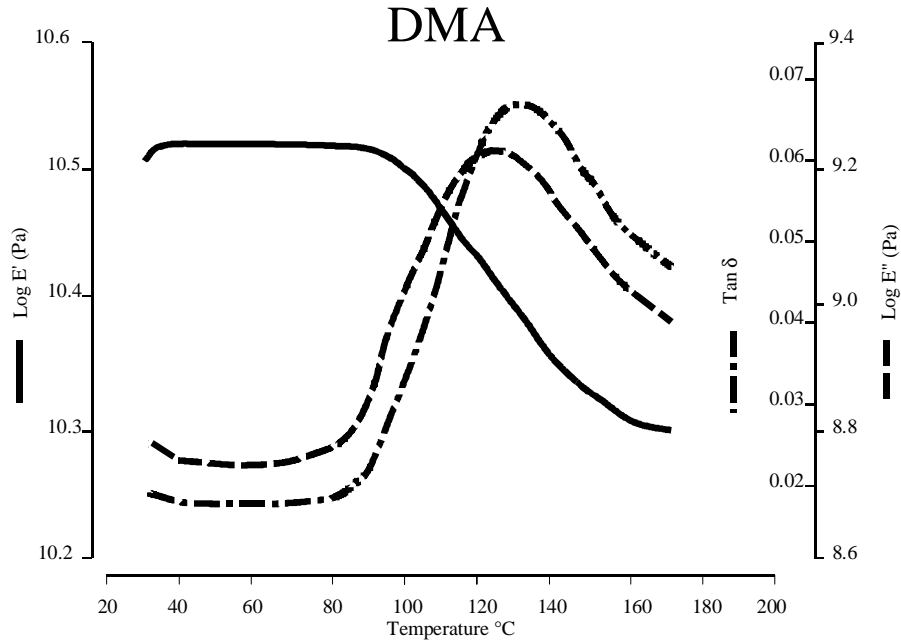


Figure 3.12 Dynamic Mechanical Analysis of Baycomp material

The DMA testing produced insights regarding precautions necessary for the specimen preparation and storage. The temperature history of the specimens had to be monitored carefully since some of the tests and preparations required temperatures that were in the vicinity of the material's glass transition temperature. At temperatures above the T_g the material's crystallinity can change and these changes will be reflected in the mechanical properties of the material. The temperature history of the specimens was kept consistent in order to maintain the same amount of crystallinity within the groups of specimens.

4. Prediction of Elevated Temperature Tensile Rupture Behavior

One of the secondary goals of this research was to develop an analytic method to predict tensile rupture behavior from bending rupture data. This method may be applicable not only to the current study, but also to other material systems. It should prove to be a valuable tool as an efficient and accurate method of quantifying the behavior of new materials. Determination of the long-term behavior under aggressive environments is of particular importance. Quite often, analysts do not consider “fiber-controlled” parameters to be time dependent. However, it has been observed that the presence of a viscoelastic matrix will indeed affect “fiber-dominated” behavior. Long-term exposure to elevated temperatures and aggressive environments degrades the performance of the matrix as a load carrying and constraining constituent.

Tensile rupture of unidirectional polymer matrix composites is a classic example of a “fiber-controlled” parameter where the matrix properties play a significant role in the long-term behavior. Typically tensile creep tests are time consuming and most load frames can only test one specimen at a time. These tests become even more complex with the introduction of elevated temperature and/or a corrosive environment. In order to obtain a statistically valid data set, many load frames must be occupied for long periods of time. It is therefore necessary to develop a method of predicting long-term tensile rupture behavior that is, first, time efficient and, second, simple. In order to satisfy the first requirement, the testing method had to be able to demonstrate the effect of the viscoelastic matrix. This condition was satisfied by selecting a bending loading in which the matrix contributes directly to the behavior of the composite system. After

experimenting with several types of bending loading, we chose a fixed-length bend-compression loading which satisfies the second requirement. The fixture is uncomplicated and can accommodate large numbers of specimens in a wide variety of environments.

The analytic model developed to predict tensile rupture behavior from the bend-compression data makes the assumption that the time rate of change of matrix shear strength is the same in both the tensile and bending situations. Two micromechanical models, which are functions of the matrix shear strength, are then used to develop a connection between the time dependent behavior of the two loadings. This procedure is discussed in the following section.

4.1 Analysis

The analysis consisted of three steps. First, micromechanics was used to model the bending rupture loading. Second, the tensile rupture loading was modeled with micromechanics. And, finally, the two micromechanical models were combined by employing our primary hypothesis to predict a rate of change of tensile strength, and thus, approximate the tensile rupture curve. The following sections describe these three steps in detail.

4.1.1 Bending Rupture Model

We observed that, for the temperature studied, when loaded in bending the failure mode is compression due to microbuckling. The bend-rupture behavior can thus be studied and modeled as a buckling compression situation. In addition to considering the microbuckling failure mode, the micromechanics model needed to take into account the matrix shear strength. After looking at several compression models, a slightly modified relation presented by Tsai and Hahn [17] was selected. Although more recent models such as Fleck and Budiansky's [18] have been developed which may characterize compression strength of composites more completely, this equation seemed to represent our data adequately and considered the necessary parameters. The derivation of this model, as presented in [17], is briefly explained below.

It is assumed that the fibers have an initial curvature as shown in Figure 4.1 and that their shape can be described by the equation

$$v_o = f_o \cdot \sin\left(\frac{\pi \cdot x}{l}\right) \quad (4.1)$$

where l is the half wavelength and f_o is the initial amplitude of fiber deflection. The application of a compressive load causes the fibers to deform to the shape

$$v = f \cdot \sin\left(\frac{\pi \cdot x}{l}\right) \quad (4.2)$$

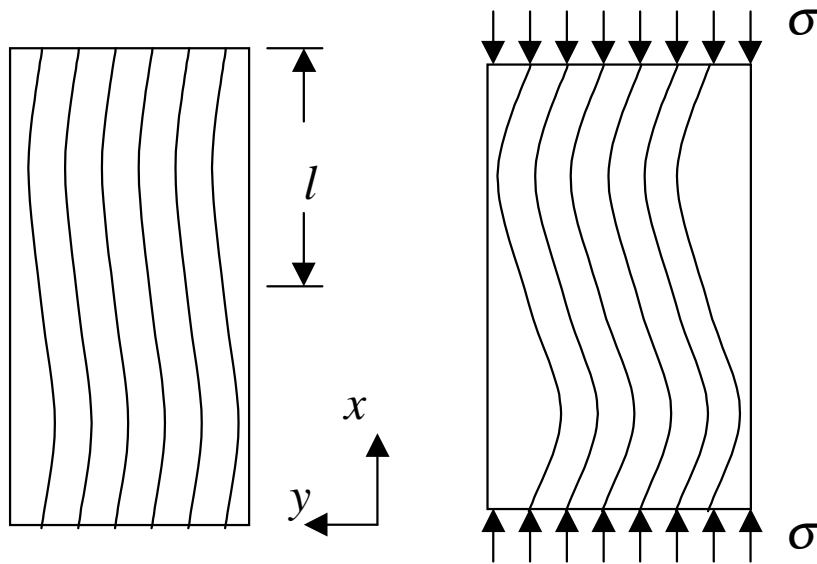


Figure 4.1 Assumed shape of local buckling in a composite in compression. Initial state (left) and deformed state (right)

Next, consider an infinitesimal representative volume element (RVE) of length dx and cross sectional area, A , as shown in Figure 4.2.

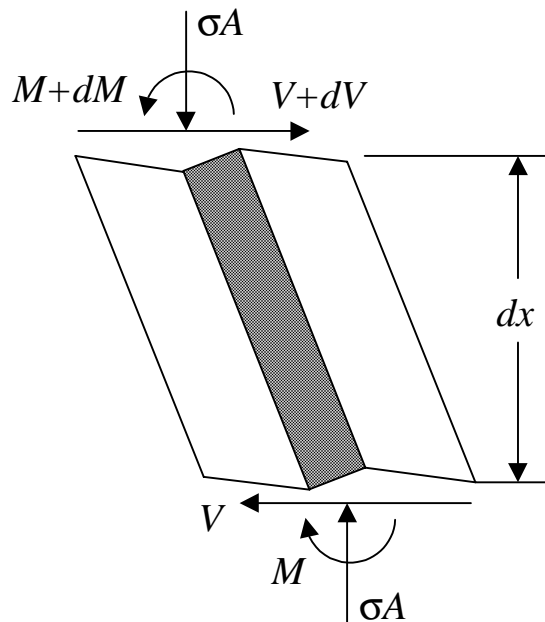


Figure 4.2 Free body diagram of the representative volume element used in the compression model

The equilibrium equation for the moments acting on the RVE is

$$\frac{dM}{dx} - V + \sigma \cdot A \cdot \frac{dv}{dx} = 0 \quad (4.3)$$

The bending moment (M) is carried by the fiber while the net shear deformation of the composite is due to V . Thus

$$M = E_f \cdot I_f \cdot \frac{d^2}{dx^2} \cdot (v - v_o) \quad (4.4)$$

$$V = A \cdot E_s \cdot I \cdot \frac{d}{dx} \cdot (v - v_o) \quad (4.5)$$

where $E_f I_f$ is the bending stiffness of the fiber and E_s is the effective shear modulus of the composite as defined in Equation (4.6).

$$\frac{1}{E_s} = \frac{1}{V_f + \eta_s \cdot V_m} \left(V_f \cdot \frac{1}{G_f} + \eta_s \cdot V_m \cdot \frac{1}{G_m} \right) \quad (4.6)$$

where V_f and V_m are the fiber and matrix volume fractions respectively, G_f and G_m are the fiber and matrix shear moduli respectively and η_s is defined by Equation (4.7).

$$\eta_s = \frac{1}{2} \left(1 + \frac{G_m}{G_f} \right) \quad (4.7)$$

Substituting the relations for the bending moment, Equation (4.4), and shear, Equation (4.5) into the equilibrium equation and noting that $I_f/A = V_f w_f^2/12$ an equation for σ is found

$$\sigma = \left[E_s + \frac{\pi^2}{12} \cdot V_f \cdot E_f \cdot \left(\frac{w_f}{l} \right)^2 \right] \cdot \left(1 - \frac{f_o}{f} \right) \quad (4.8)$$

where w_f is the width of the fibers. For composites the value $w_f/l \ll 1$; therefore, the second term in the brackets can be neglected so that Equation (4.8) becomes

$$\sigma = [E_s] \cdot \left(1 - \frac{f_o}{f}\right) \quad (4.9)$$

Equation (4.9) relates the compressive stress and the amplitude of the fiber deflection (f). One can see that as σ increases, so too will f . This process continues until f reaches a critical value, f_c , at which the composite fails. The compressive strength is then written as

$$X_c = [E_s] \cdot \left(1 - \frac{f_o}{f_c}\right) \quad (4.10)$$

The composite can fail due to local shear failure or bending failure of the fibers. If the failure mode is shear, the maximum local shear stress can be calculated from Equation (4.5). f_c is then the value of f at which the maximum shear stress is equal to the shear strength of the composite.

$$f_c = f_o + \frac{l}{\pi} \cdot \frac{S}{E_s} \quad (4.11)$$

If the failure mode is fiber bending, failure occurs when the maximum bending stress reaches the fiber strength X_f . For this case, f_c can be found using a technique similar to that applied to the shear failure

$$f_c = f_o + \frac{2 \cdot l}{w_f} \cdot \frac{l}{\pi^2} \cdot \frac{X_f}{E_f} \quad (4.12)$$

Since $2l/w_f$ is much greater than unity, f_c will be largest when calculated for fiber bending failure. The compressive failure of the composite is therefore caused by local shear failure and the compressive strength can then be written as

$$X_c = \frac{E_s}{1 + \frac{f_o \cdot \pi}{l} \cdot \frac{E_s}{S}} \quad (4.13)$$

Equation (4.13) was further simplified for use in our model by substituting for f_o and l a single initial fiber misalignment angle, ϕ . The geometry of this approximation is shown in Figure 4.3.

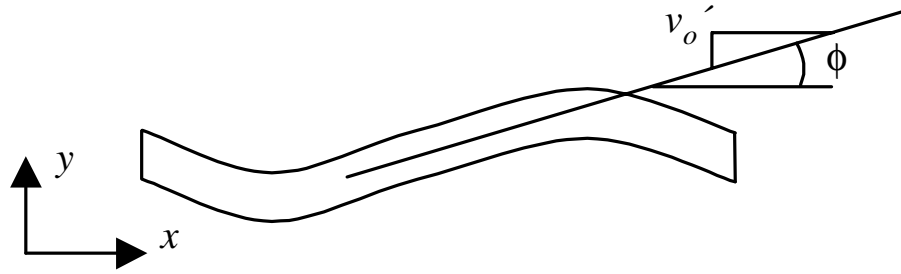


Figure 4.3 Geometry of initial fiber misalignment used to simplify the compression strength model

The slope of the initial fiber shape is

$$v_o' = f_o \cdot \frac{\pi}{l} \cdot \cos\left(\frac{\pi \cdot x}{l}\right) \quad (4.14)$$

and has a maximum value of $f_o \pi / l$ which corresponds to the greatest fiber misalignment angle. This maximum slope is equal to $\tan(\phi)$ which can be approximated as ϕ for small angles, thus

$$\phi = \frac{f_o \cdot \pi}{l} \quad (4.15)$$

Substituting this equation for ϕ into the compressive strength Equation (4.13), a simplified relation for the compressive strength is found to be

$$X_c = \frac{E_s}{1 + \phi \cdot \frac{E_s}{S}} \quad (4.16)$$

where E_s is the effective shear modulus of the composite, ϕ is the initial fiber misalignment angle (which we determined to be about 3° [34]), and S is the composite shear strength.

4.1.2 Tensile Rupture Model

Since the tensile rupture of the unidirectional material was a strictly tensile situation, it was modeled directly with a micromechanics tensile model. It was necessary to select a micromechanics relation that takes into account the matrix shear strength. For this task a global load-sharing tensile strength model was selected. This model was originally developed by Curtin [16] to study ceramic matrix composites, but it also appeared to represent the composite material under study adequately. The derivation of this model, as presented in [1], is outlined below.

Consider a matrix of modulus E_m reinforced with uniaxial fibers of volume fraction V_f , radius r , Modulus E_f , characteristic fiber strength, σ_o , at a reference length (L), and Weibull shape parameter, m , of the statistical distribution of fiber strengths. Until the point of matrix cracking, the composite modulus is $E = V_f E_f + (1-V_f) E_m$. After matrix cracking, the load is born equally by the fibers in an arbitrary matrix crack plane. Looking at a single matrix crack plane at the applied load σ , the average stress per fiber is σ / V_f . This load is partially supported by fibers with no breaks within $\pm l_f$ (the fiber slip length) of the matrix crack. The remainder of the load is carried by fibers that are broken within a single slip length of the crack plane. The slip length is the distance along the fiber that the interfacial shear strength, τ , must act upon to build the fiber stress up to

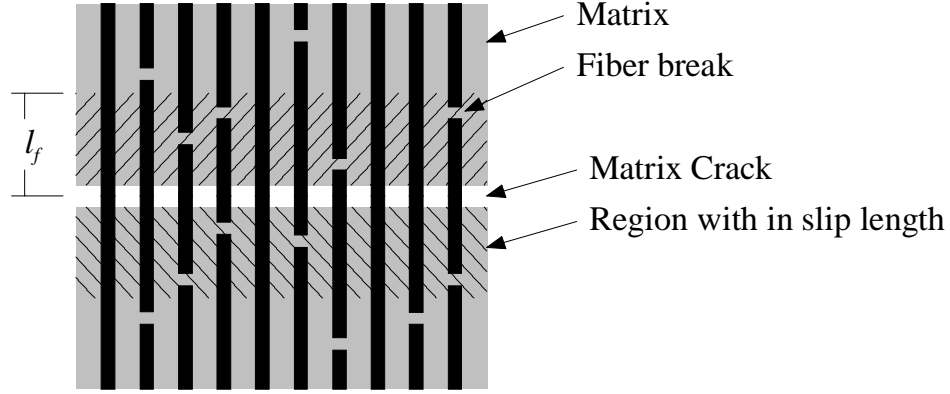


Figure 4.4 Arrangement of fiber breaks in the vicinity of a matrix crack

its uncracked value. Figure 4.4 provides a visual description of the situation being modeled. For frictional sliding of the fibers near a break, the slip length l_f is given by

$$l_f = \frac{r \cdot \sigma_f(l_f)}{2 \cdot \tau} \quad (4.17)$$

where $\sigma_f(l_f)$ is the fiber stress previously existing at l_f away from the break.

Next, the stress carried by the unbroken fibers is denoted as T and the fraction of fibers broken within $\pm l_f$ by $q(l_f)$ so that

$$\frac{\sigma}{V_f} = T(1 - q(l_f)) + \frac{2 \cdot \tau}{r} \cdot \langle L(T) \rangle \cdot q(l_f) \quad (4.18)$$

The first term in Equation (4.18) represents the load carried by the fraction $1 - q$ of unbroken fibers and the second term is the average load carried by the q broken fibers due to shear stress τ acting over the average pullout length $\langle L(T) \rangle$. By recognizing that

$$l_f = \frac{r \cdot T}{2 \cdot \tau} \quad (4.19)$$

and substituting into equation (4.18) we have

$$\frac{\sigma}{V_f} = T \left[1 - \left(1 - \frac{\langle L(T) \rangle}{l_f} \right) \cdot q(l_f) \right] \quad (4.20)$$

Two additional approximations are now made. First, assume that at the value of T which maximizes Equation (4.20) the probability of having two breaks on the same fiber within $\pm l_f$ of the matrix crack is small. Therefore the average pullout length is given by $\langle L(T) \rangle = l_f / 2$ and Equation (4.20) becomes

$$\frac{\sigma}{V_f} = T \left(1 - \frac{1}{2} \cdot q(l_f) \right) \quad (4.21)$$

Second, approximate $q(l_f)$ by the fraction of breaks occurring in a gage length $2 l_f$. Thus

$$q(l_f) \approx \frac{2 \cdot l_f}{L_o} \cdot \left(\frac{T}{\sigma_o} \right)^m \quad (4.22)$$

Substituting Equation (4.19) into Equation (4.22) and then the result into Equation (4.21) and finally maximizing with respect to T , an approximation for the tensile strength is found

$$\sigma_t = V_f \cdot \sigma_o^{\frac{m}{m+1}} \cdot \left(\frac{S \cdot L}{r} \right)^{\frac{1}{m+1}} \cdot \left(\frac{2}{m+2} \right)^{\frac{1}{m+1}} \cdot \frac{m+1}{m+2} \quad (4.23)$$

where V_f is the fiber volume fraction, σ_o is the characteristic fiber strength at a reference length (L), m is the Weibull shape parameter of the statistical distribution of fiber strengths, r is the fiber radius, and S is the interfacial shear strength (which in this analysis was approximated by the matrix shear strength).

4.1.3 Predict Tensile Rupture

The third step in the analysis is to apply our primary hypothesis to combine the two models for compressive and tensile strength. As stated previously, the primary hypothesis for this analysis is: for a given normalized stress level, the rate of change of

matrix shear strength with respect to time will be the same for both compression and tensile loading. We also assume that all other material parameters and the environmental test conditions associated with the micromechanical models remain constant with time.

Differentiation of the compression strength model, Equation (4.16), with respect to time gives the time rate of change of compression strength

$$\frac{dXc}{dt} = \frac{Es^2 \cdot \phi}{(S + \phi \cdot Es)^2} \cdot \frac{dS}{dt} \quad (4.24)$$

Applying the same procedure to the tensile strength model, Equation (4.23), we find the rate of change of tensile strength with respect to time

$$\frac{dXt}{dt} = V_f \cdot \sigma_o^{\frac{m}{m+1}} \cdot \left(\frac{L}{r}\right)^{\frac{1}{m+1}} \cdot S^{-\frac{m}{m+1}} \cdot \left(\frac{2}{m+2}\right)^{\frac{1}{m+1}} \cdot \frac{1}{m+2} \cdot \frac{dS}{dt} \quad (4.25)$$

Next, considering our primary hypothesis and our controlled experiments, we equate the rate of change of the matrix shear strength (dS/dt) in the compression and tensile models. A ratio (Rs) of the time rate of change of tensile to compression strength is then determined

$$Rs = \frac{\frac{dXt}{dt}}{\frac{dXc}{dt}} = \frac{V_f \cdot \sigma_o^{\frac{m}{m+1}} \cdot \left(\frac{L}{r}\right)^{\frac{1}{m+1}} \cdot S^{-\frac{m}{m+1}} \cdot \left(\frac{2}{m+2}\right)^{\frac{1}{m+1}} \cdot \frac{1}{m+2}}{\frac{Es^2 \cdot \phi}{(S + \phi \cdot Es)^2}} \quad (4.26)$$

Taking into account values for the material parameters of the fibers and matrix at different temperatures the nature of this result can be studied. The properties for AS-4 carbon fibers (which were assumed to remain constant with temperature) are shown in Table 4.1 [2].

Table 4.1 Properties of AS-4 carbon fiber

Property	Value
Fiber volume fraction (V_f)	0.404
Tensile Modulus (E_f)	34.08 Msi
Shear Modulus (G_f)	4.06 Msi
Characteristic strength (σ_o)	760.9 ksi
Reference length (L)	1.0 mm (0.039 in)
Weibull shape parameter (m)	10.65
Fiber radius	1.378 E-4 in

The temperature dependent properties of the matrix are illustrated as functions of temperature in Figure 4.5 [6] and Figure 4.6 [5].

It was assumed that the matrix can be modeled as a homogenous material, thus the matrix shear modulus was approximated with the basic mechanics of materials relation

$$G_m = \frac{E_m}{2 \cdot (1 + \nu_m)} \quad (4.27)$$

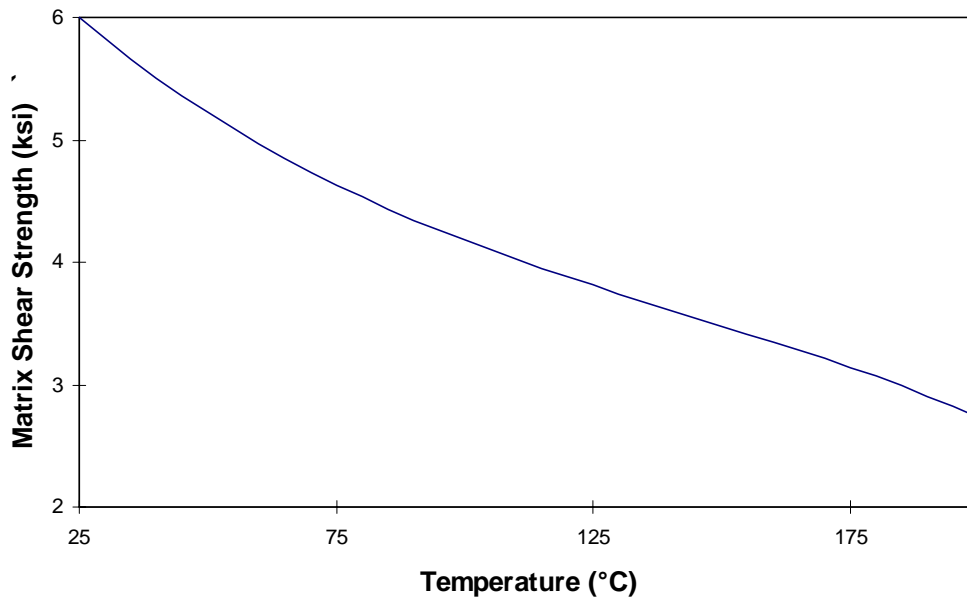


Figure 4.5 Shear strength of PPS matrix vs. Temperature

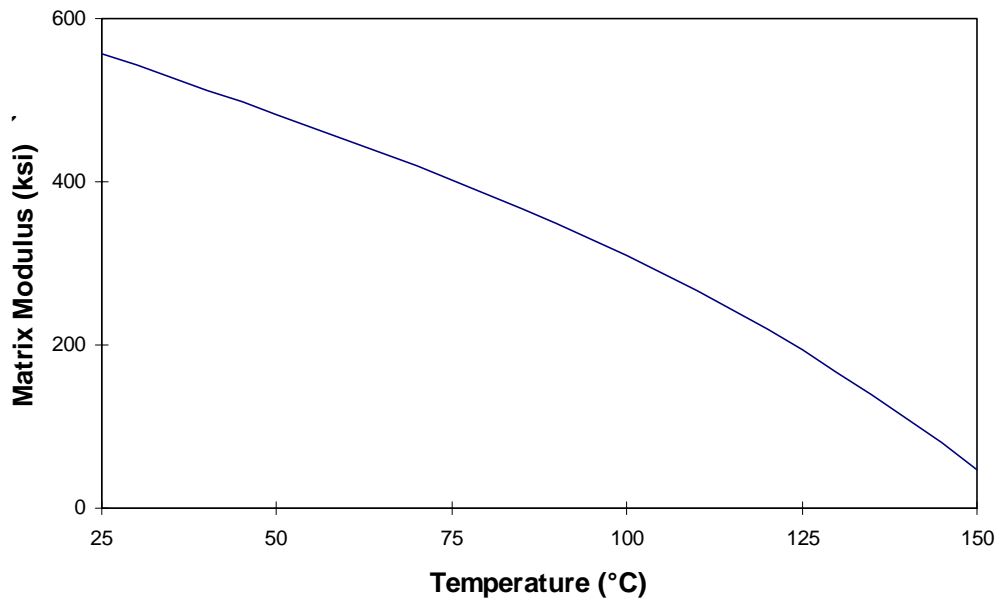


Figure 4.6 Modulus of PPS matrix vs. Temperature

Considering the data presented above and Equation (4.26) R_s is calculated at different temperatures.

Table 4.2 Slope ratio (R_s) at different temperatures

Temperature (°C)	R_s
140	0.927
120	0.568
90	0.433
50	0.348

We can observe from Table 4.2 that as temperature decreases the slope of the tensile curve will be increasingly less than that of the compression curve. This conclusion is rational since at lower temperatures the slope of the tensile rupture curve should in fact be minimal.

For a given temperature, this ratio can be used to estimate the slope of the tensile curve for each corresponding stress level of the bend-rupture curve. We will now

demonstrate how the ratio is used to produce an estimate of the tensile rupture curve. Beginning with the results of the bend-compression tests, Figure 4.7, which were fit with a curve from Kachanov [36] of the form

$$t = \frac{1}{(n_b + 1) \cdot A_b \cdot \sigma^{n_b}} \quad (4.28)$$

where t is the time to failure in hours, σ is normalized stress and A_b and n_b are constants determined via curve fitting. The subscript b denotes bending; an equation of the same form will be used to represent the tensile rupture curve in which case a subscript t will be used. This is a familiar damage accumulation curve selected primarily because the general shape of the curve matched the data. Equation (4.28) can be rearranged to find the applied stress as a function of the failure time

$$\sigma(t) = [t \cdot A_b \cdot (n_b + 1)]^{-\frac{1}{n_b}} \quad (4.29)$$

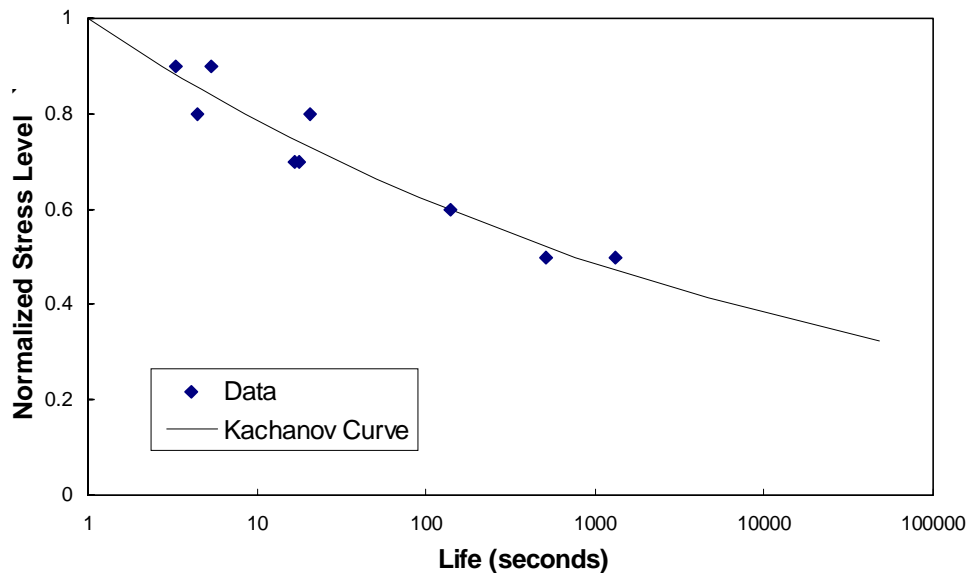


Figure 4.7 Bend-compression rupture data at 90°C and curve fit

Then differentiating Equation (4.29) and recognizing that the applied stress σ is equivalent to the failure stress Xc , we can write an equation for the slope of the curve

$$\frac{dXc}{dt} = \frac{-[t \cdot A_b \cdot (n_b + 1)]^{\frac{1}{n_b}}}{n_b \cdot t} \quad (4.30)$$

Based on our primary hypothesis we can write

$$\frac{dXt}{dt} = R_s \cdot \frac{dXc}{dt} \quad (4.31)$$

and then assuming that the tensile rupture curve can be approximated with a curve of the same form as the bending rupture Equation (4.31) becomes

$$\frac{-[t \cdot A_t \cdot (n_t + 1)]^{\frac{1}{n_t}}}{n_t \cdot t} = R_s \cdot \frac{-[t \cdot A_b \cdot (n_b + 1)]^{\frac{1}{n_b}}}{n_b \cdot t} \quad (4.32)$$

Given A_b and n_b it is possible to solve exactly for A_t and n_t

$$A_t = A_b \cdot R_s^{-n_b} \quad (4.33)$$

$$n_t = n_b \quad (4.34)$$

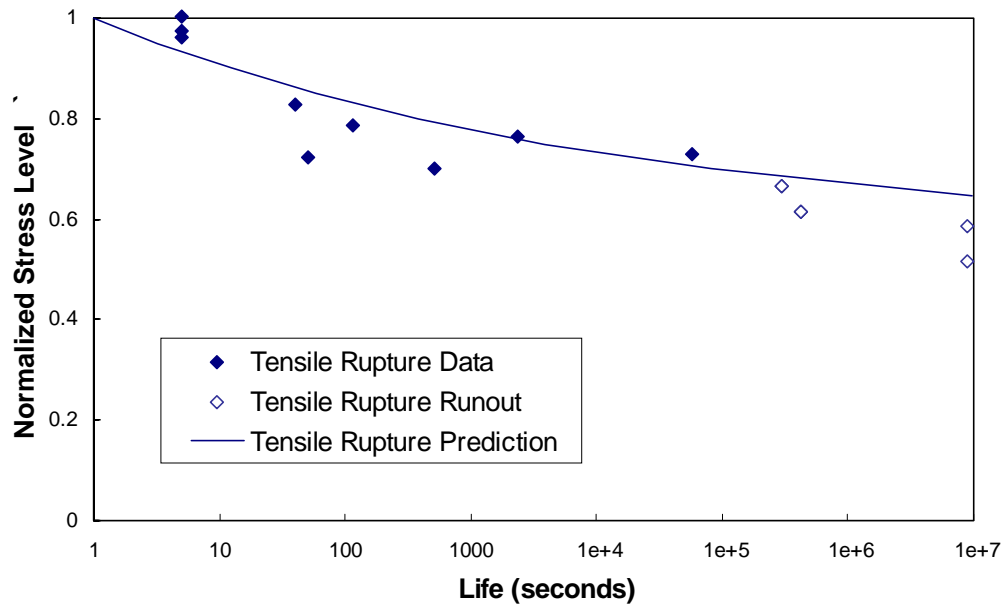


Figure 4.8 Comparison of tensile rupture curve prediction and tensile rupture data

In addition to satisfying the slope requirement, the tensile rupture curve must also pass through unity at time equal to zero (which was approximated by one second). This is accomplished by adding a constant which shifts the curve along the vertical axis. The tensile rupture curve predicted through this procedure and experimentally obtained tensile rupture data are displayed in Figure 4.8. As Figure 4.8 demonstrates, the tensile behavior was estimated accurately via the presented analysis for this particular material at 90°C.

4.2 Conclusions for the Tensile Rupture Prediction

A technique has been developed which enables the efficient and accurate prediction of tensile rupture behavior of a unidirectional polymer matrix composite. This prediction is derived from bend compression data that are considerably more easily and quickly obtained than conducting the tensile rupture tests themselves. The derivation is based on the assumption that the rate of change of the matrix shear strength with time at temperature is the same in both tensile and bending loading. Beside the direct use of such tensile rupture predictions, it is possible to use the results in conjunction with room temperature fatigue data to predict elevated temperature tensile fatigue, as we will show in Chapter 5. It may also be possible to use a similar technique to determine the viscoelastic behavior of these materials. The micromechanical approach used here may have broader applicability, especially for other failure modes. It should also be noted that this method has the effect of “accelerating” the characterization of materials, of particular value to certification and component development efforts. However, the generality of the method must be established by further research.

5. Discussion and Verification of Elevated Temperature Life Prediction

The service life model for the flexible pipe composite armor was constructed with MRLife, a performance simulation code for material systems developed by the Materials Response Group at Virginia Tech [1]. This program uses experimental data and analytical tools to predict the long-term behavior of a composite. This chapter provides an overview of the fundamental concepts of the MRLife Code including several modifications to the code designed to better represent the loading and material under study. In order to validate the code and new concepts, experimental data is compared to life prediction results produced by the code.

5.1 MRLife Overview [37]

The MRLife life prediction scheme is based upon damage accumulation in composites. The basic principles of this scheme are described as follows. We begin our analysis by postulating that remaining strength may be used as a damage metric. We next assume that the remaining strength may be determined (or predicted) as a function of load level and some form of generalized time. For a given load level, a particular fraction of life corresponds to a certain reduction in remaining strength. We claim that a particular fraction of life at a second load level is equivalent to the first if and only if it gives the same reduction in remaining strength, as illustrated in Figure 5.1. In the case of Figure 5.1, time t_1 at an applied stress level S_a^1 is equivalent to time t_2 at stress level S_a^2 because it gives the same remaining strength. In addition, the remaining life at the second load

level is given by the amount of generalized time required to reduce the remaining strength to the applied load level. In this way, the effect of several increments of loading may be accounted for by adding their respective reductions in remaining strength. For the general case, the strength reduction curves may be nonlinear, so the remaining strength and life calculations are path dependent.

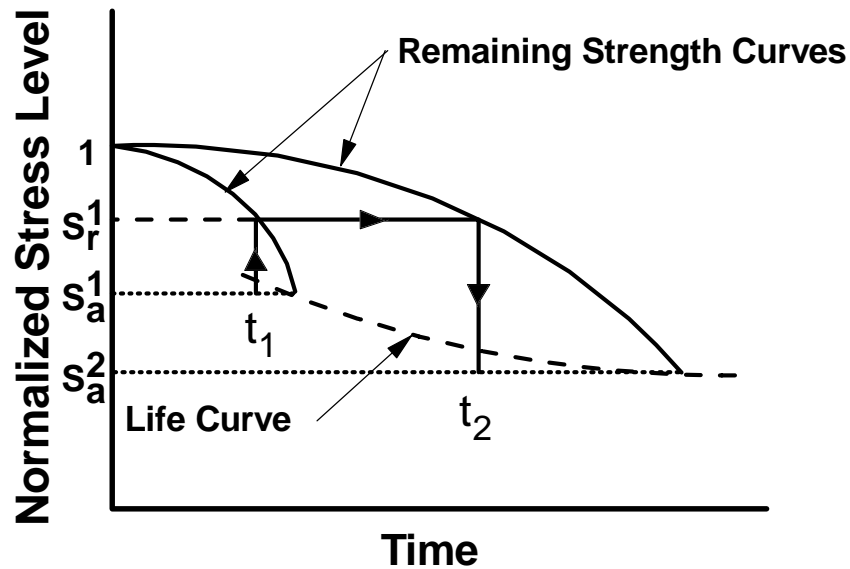


Figure 5.1 The use of remaining strength as a damage metric

Our next step in the analysis is to postulate that normalized remaining strength (our damage metric) is an internal state variable for a damaged material system. This normalized remaining strength is based upon the selection of an appropriate failure criterion (such as maximum stress or Tsai-Hill) which is a scalar combination of the principal material strengths and applied stresses in the critical element. In this way we are able to consider a single quantity rather than the individual components of the strength tensor. We denote this failure function by Fa . We next construct a second state variable, the continuity [36], defined as $(1-Fa)$ and denote it by ψ . We shall attempt to

define our remaining strength and life in terms of ψ . To do so, we assume that the kinetics are defined by a specific damage accumulation process for a particular failure mode, and assign different rate equations to each of the processes that may be present.

As an example, let us consider a common kinetic equation (a power law) such that

$$\frac{d\psi}{d\tau} = A\psi^j \quad (5.1)$$

where j is a material constant and τ is a generalized time variable defined by

$$\tau = \frac{t}{\hat{\tau}} \quad (5.2)$$

and $\hat{\tau}$ is the characteristic time for the process at hand. This characteristic time could be a creep rupture life, a creep time constant, or even a fatigue life, in which case

$$\tau = \frac{n}{N} \quad (5.3)$$

where n is the number of fatigue cycles and N is the number of cycles to failure at the current applied loading conditions. It is also possible to combine time and cycle dependent processes by expressing the characteristic time as

$$\frac{1}{\hat{\tau}} = R \frac{1}{t_{rupture}} + (1 - R) \frac{1}{t_{fatigue}}; \quad t_{fatigue} = \frac{N_{fatigue}}{\nu} \quad (5.4)$$

where R is defined as $\frac{\sigma_{min}}{\sigma_{max}}$ of the fatigue process, ν is the fatigue frequency, $N_{fatigue}$ is the number of cycles to fatigue failure, and $t_{rupture}$ is the time to failure for the time dependent process. It can be seen that this concept is correct in its limits; when R is 1 (pure rupture) $\hat{\tau}$ is the time to rupture failure and when $R = 0$ (pure fatigue) $\hat{\tau}$ is the time required for fatigue failure to occur at the given frequency. This concept was added to the code to

model the combined the effects of fatigue and time at elevated temperature on the current material under study.

Next, we rearrange Equation (5.1) and integrate so that we have

$$\int_{\psi_0}^{\psi_i} d\psi = A \int_0^{\tau_i} (\psi(\tau))^j d\tau \quad (5.5)$$

If we set $A=-1$ and $j = 1$, we arrive at

$$\psi_i - \psi_0 = 1 - Fa_i - (1 - Fa_0) = -\Delta Fa = -\int_0^{\tau_i} (1 - Fa(\tau)) d\tau \quad (5.6)$$

Then we define our normalized remaining strength, Fr so that

$$Fr = 1 - \Delta Fa = 1 - \int_0^{\tau} (1 - Fa(\tau)) d\tau \quad (5.7)$$

In such a form, failure is predicted at the point at which the remaining strength equals the applied load ($Fr = Fa$).

5.2 Code Validation

We will now apply the damage accumulation scheme previously described to predict the elevated temperature fatigue behavior of the material under study and then compare these predictions to experimental data. The first step in implementing the code for this task is to characterize the time dependent behavior of the failure process. In our case this is tensile rupture at an elevated temperature of 90°C.

The general representation for strength reduction as a function of time in MRLife is

$$R = 1 + A \cdot \log(t) + B \cdot \log(t)^2 + C \cdot \log(t)^3 + D \cdot \log(t)^4 \quad (5.8)$$

where R is the remaining strength fraction, the elapsed time (t) is in hours, and A, B, C, D are material constants determined via curve fitting. Due to the inherent shape of this curve, it could not adequately represent the rupture data; consequently, MRLife was modified to use a strength reduction equation presented by Kachanov [36] of the form

$$t_{rupture} = \frac{I}{(n+1) \cdot A \cdot \sigma^n} \quad (5.9)$$

where σ is the normalized initial stress and $t_{rupture}$ is the time to rupture in hours. A and n are constants determined through curve fitting. Setting σ equal to R (the remaining strength fraction) Equation (5.9) can be rewritten in the form used in MRLife

$$R = \left[\frac{I}{(n+1) \cdot A \cdot t_{rupture}} \right]^{\frac{1}{n}} \quad (5.10)$$

Equation (4.4) is then fit, using a least squares method, to the 90°C tensile rupture data

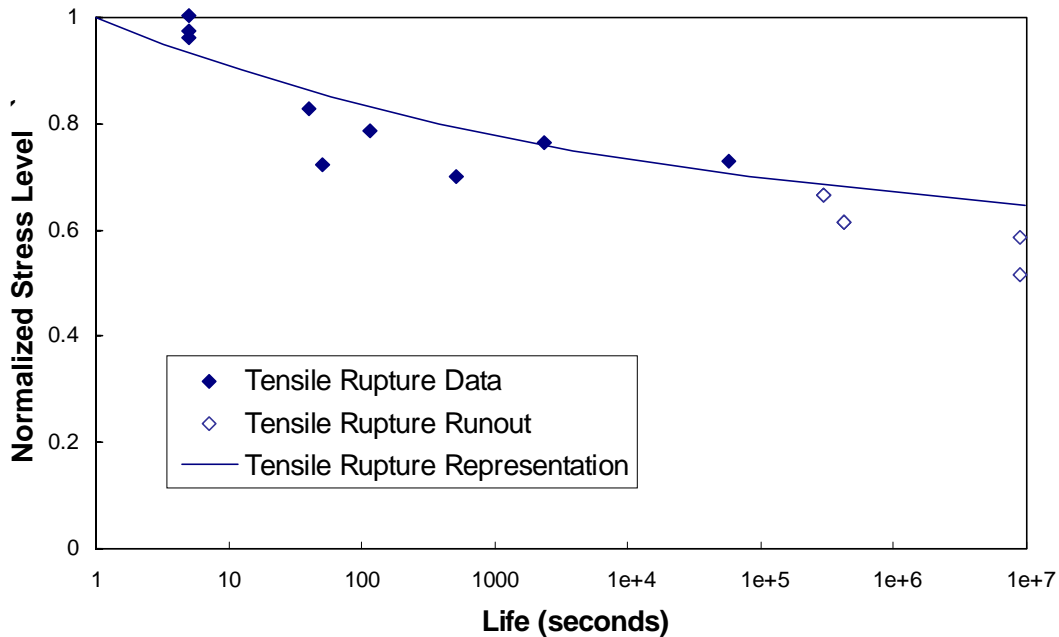


Figure 5.2 Tensile rupture curve fit and data

presented in Section 3.6. The values of A and n were determined to be 2467 and 36.7 respectively. The tensile rupture curve fit and data are shown in Figure 5.2.

Next, the fatigue effect of the combined loading is characterized. The room temperature fatigue data given in Section 3.3 were fit with a conventional S-N curve of the form

$$\frac{S}{S_{ULT}} = A_n + B_n (\log N)^{P_n} \quad (5.11)$$

The data and curve are shown in Figure 5.3. The constants were found to be: $A_n=0.9207$, $B_n=-0.0189$, and $P_n=1$.

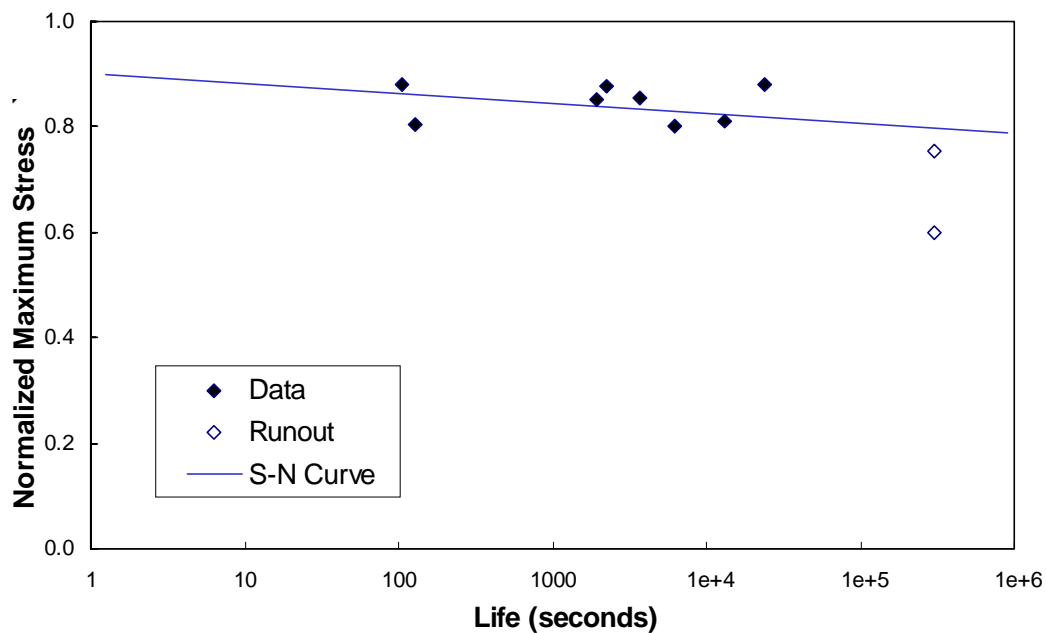


Figure 5.3 Room temperature fatigue fit and S-N curve fit

Finally, the effects of time at elevated temperature and fatigue are combined by defining a characteristic time as described in Section 5.1. For any given normalized stress level, a rupture time and a fatigue time can be determined from the two previous curve fits. These times in conjunction with the R-ratio of the process are then used to compute

the characteristic time with Equation (5.4). The generalized time is in turn then computed with Equation (5.2) and input into the evolution equation (5.7) to predict time to failure for the given stress level.

The MRLife prediction for the combined loading and the 90°C fatigue data, shows a good correlation between the prediction and data (Figure 5.4). This verifies the technique for predicting the combined effects of time and cyclic processes for the material under study. The final step is then to apply MRLife to predict the life of the flexible pipe composite armor in an ocean environment as will be described in the following chapter.

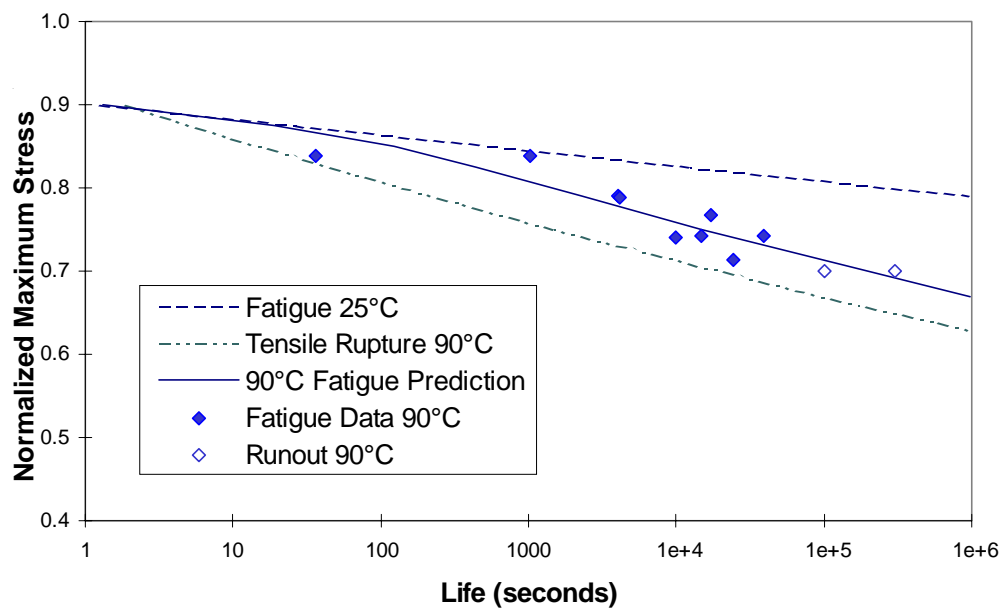


Figure 5.4 Comparison of elevated temperature fatigue prediction and 90°C fatigue data

6. Composite Armor Life Prediction

A service life model for the composite helical armor of an unbonded flexible pipe has been developed. The loading and environmental conditions simulated by the model are derived from the pipe's expected service as a riser for an offshore oil platform. This chapter discusses the life prediction process in the following sections:

- Determine the forces experienced by the composite armor via a stress analysis of the flexible pipe structure.
- Integrate the loading history of the pipe due to an ocean environment into the MRLife code to predict the armor life.
- Conduct several parameter studies of a flexible pipe in a hypothetical environment. These analyses highlight certain loadings and conditions which are particularly detrimental to the life of the material.

6.1 Unbonded Flexible Pipe Stress Analysis

In order to develop a life prediction model for the flexible pipe, it is necessary to determine the stresses that the composite armor will experience. A technique suggested by Claydon et. al. [25] was incorporated to accomplish this task. This section presents a cursory review of the pipe stress analysis. The analysis was conducted with Mathcad 6.0 and the entire worksheet is displayed in Appendix A.

Figure 6.1 displays the structure of a typical unbonded flexible pipe. Each layer can be classified as one of two types: a cylindrical homogeneous layer, or a helically wound tendon layer. The stress analysis is initiated by first determining relations for the

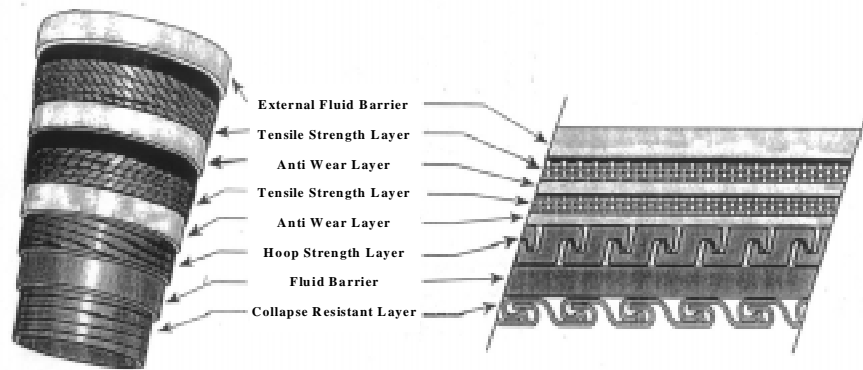


Figure 6.1 Structure of an unbonded flexible pipe with composite tensile strength (armor) layers

axial and radial stiffness of each layer. The pipe stiffness is then calculated considering equilibrium and compatibility of the entire pipe. We can then back-solve to find the stresses in each individual layer for a given axial force, pipe radius of curvature and pressure differential between the inside and outside of the pipe.

The assumptions taken into account in the derivation of this analysis are noted below.

- All stiffness relationships assume small displacements and strains.
- The stiffness formulation considers only axial tension and pressure in the pipe. The stresses will thus be constant around the pipe circumference. Stresses produced by pipe bending are evaluated separately and then superimposed on the initial stresses.
- The cylindrical layers are modeled with conventional elastic thin-walled theory.
- It is assumed that adjacent layers will constrain the helical layers from rotating about their local axial axis.
- The through-thickness strains of the individual layers are neglected. Radial compatibility thus requires all layers to have the same radial displacement.

- For the calculation of radial equilibrium, layer thicknesses are ignored. The total pressure change through the pipe is then the sum of the pressure differential over each layer.
- Additional stress produced by the curvature of the helical tendons are neglected. The relatively large bend radius and minimal thickness of the helical tendons cause this stress to be very low (less than 1% of the total stress) for the pipe material and geometry under consideration.

6.1.1 Cylindrical layer stiffness

The cylindrical layer stiffness is analyzed with conventional elastic thin-walled theory. Figure 6.2 illustrates the applied forces and resulting stresses within a cylindrical layer section. Considering equilibrium of the section and elastic stress-strain

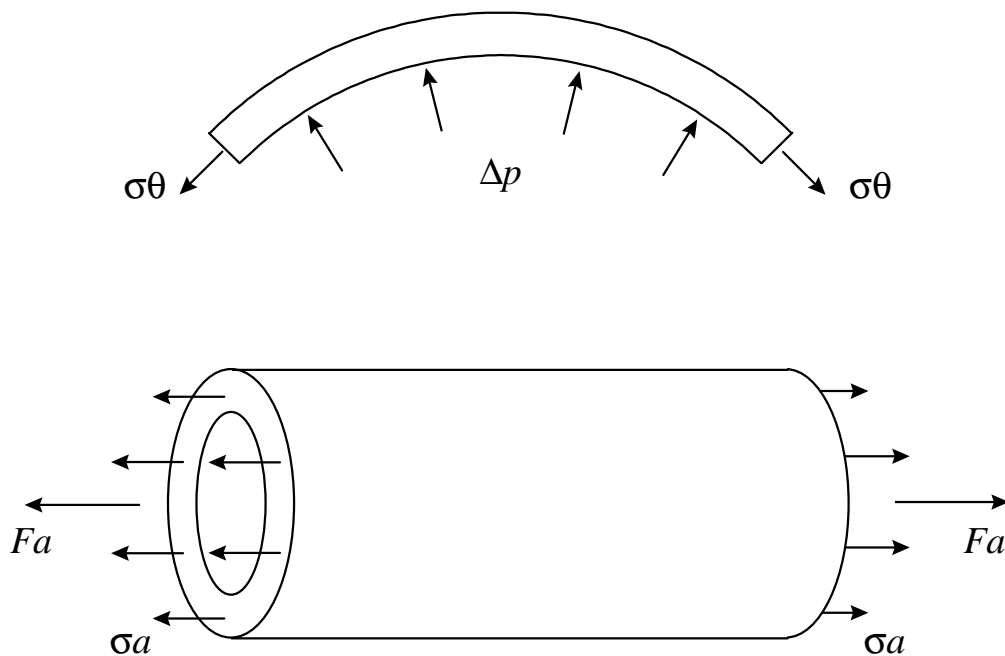


Figure 6.2 Stresses and loads on a cylindrical layer

relationships, equations for the pressure differential through the layer (6.1) and axial force supported by the layer (6.2) are derived as functions of the radial displacement (Δr) and axial strain (Δl).

$$\Delta p = \left(\frac{Et}{r^2(1-\nu^2)} \right) \Delta r + \left(\frac{\nu Et}{r(1-\nu^2)} \right) \Delta l \quad (6.1)$$

$$Fa = \left(\frac{\nu 2\pi Et}{1-\nu^2} \right) \Delta r + \left(\frac{2\pi Ert}{1-\nu^2} \right) \Delta l \quad (6.2)$$

E and ν are the elastic modulus and Poisson's Ratio of the layer material respectively, r is the mean radius of the layer and t is the layer thickness.

6.1.2 Helical layer stiffness

The forces acting on a helical tendon segment are shown in Figure 6.3. This loading is constant along the length of the tendon since axial tension and internal pressure are assumed to be constant for the whole pipe. Via a rather complex analysis which

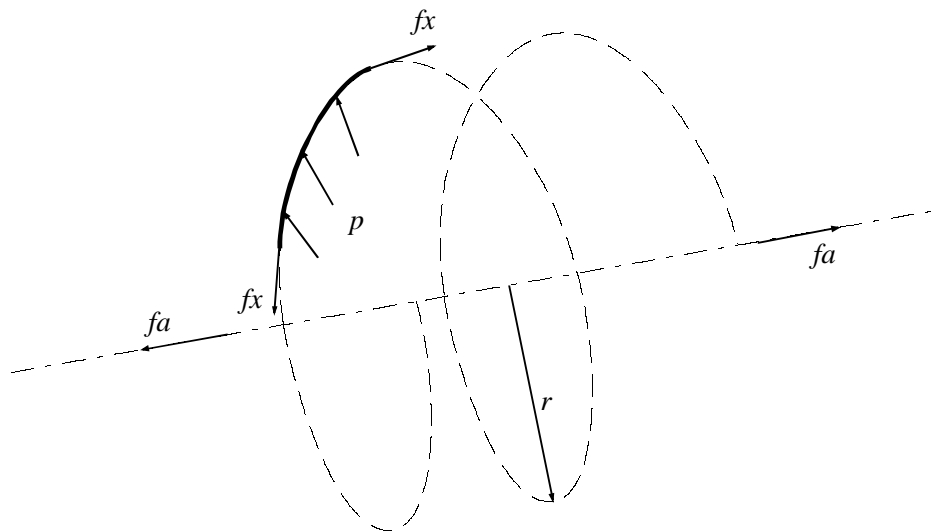


Figure 6.3 Helical layer geometry and applied forces

considers force and moment equilibrium of the section, changes in curvature and twist of the segment, axial strain of the segment and finally a kinematic constraint for the helix, relations for the pressure differential through the layer (6.3) and axial force supported by the layer (6.4) are determined. As with the cylindrical layer relations, these equations are functions of the radial displacement and axial strain.

$$\Delta p = \frac{n \tan(\alpha)}{2\pi r} \left\{ \left[\left(\frac{\sin^3(\alpha) \cos^2(\alpha) \cos(2\alpha)}{r^4} EI \right) - \left(\frac{2 \cos^4(\alpha) \sin^3(\alpha)}{r^4} GJ \right) + \left(\frac{\sin^3(\alpha)}{r^2} EA \right) \right] \Delta r \right. \\ \left. + \left[\left(\frac{-2 \sin^3(\alpha) \cos^4(\alpha)}{r^3} EI \right) - \left(\frac{\sin^3(\alpha) \cos^2(\alpha) (\sin^2(\alpha) - \cos^2(\alpha))}{r^3} GJ \right) + \left(\frac{\sin(\alpha) \cos^2(\alpha)}{r} EA \right) \right] \Delta l \right\} \quad (6.3)$$

$$fa = \frac{Fa}{n} = \left\{ \left[\left(\frac{-\sin^4(\alpha) \cos(\alpha) \cos(2\alpha)}{r^3} EI \right) + \left(\frac{2 \cos^3(\alpha) \sin^4(\alpha)}{r^3} GJ \right) + \left(\frac{\sin^2(\alpha) \cos(\alpha)}{r} EA \right) \right] \Delta r \right. \\ \left. + \left[\left(\frac{2 \sin^4(\alpha) \cos^3(\alpha)}{r^2} EI \right) + \left(\frac{\sin^4(\alpha) \cos(\alpha) (\sin^2(\alpha) - \cos^2(\alpha))}{r^2} GJ \right) + (\cos^3(\alpha) EA) \right] \Delta l \right\} \quad (6.4)$$

E , G and ν are the elastic modulus, shear modulus and Poisson's Ratio respectively of the helical tendon, I , J and A are the moment of inertia, polar moment of inertia and cross sectional area respectively of the helical tendon, α is the wrap angle, r is the mean radius of the layer and n is the multiplicity of the helix.

6.1.3 Total pipe stiffness

We now use equilibrium and compatibility of the pipe to combine the changes in pressure through each layer and the axial force in each layer. The net pressure change through the pipe is the sum of the pressure differentials of all the layers and can, in turn, be written as a function of the radial displacement and axial strain as shown in Equation (6.5).

$$P = \sum \Delta p_i = \left(\sum p_r \right) \Delta r + \left(\sum p_l \right) \Delta l \quad (6.5)$$

Equation (6.6) gives the total axial force derived in a similar fashion.

$$F = \sum F a_i = \left(\sum f_r \right) \Delta r + \left(\sum f_l \right) \Delta l \quad (6.6)$$

These two equations are then solved simultaneously to determine the radial displacement and axial strain of the pipe. To calculate the force supported by the individual helical tendons (fx) we back-solve Equations (6.4) and (6.3) for fa and p and then solve for fx via Equation (6.7).

$$fx = fa \cos(\alpha) + rp \sin(\alpha) \quad (6.7)$$

6.1.4 Stresses due to pipe bending

The additional stress in the layers produced by bending of the pipe will vary around its circumference; being greatest for the helical tendons located at an angle of $\pi/2$ from the neutral bending axis. This maximum additional stress will be considered in the life prediction analysis in order to produce a conservative result. If the coefficient of friction and the contact pressure between the layers combine to produce a frictional force large enough to prevent the layers from slipping in relation to one another, the pipe will essentially perform as a “bonded” pipe. The additional stress in the helical layers for this “no slip” condition can be modeled with the Engineer’s Theory of Bending, Equation (6.8).

$$\sigma_a = \frac{Er \sin(\phi)}{R} \cos^2(\alpha) \quad (6.8)$$

where E is the layer modulus, r is the mean layer radius, ϕ is the angle from the neutral bending axis of the pipe, R is the pipe radius of curvature and α is the helix wrap angle.

If slipping between the layers does occur, Equation (6.9) gives the additional helical tendon stress due to friction forces.

$$\sigma_f = (\mu_{i-1}p_{i-1} + \mu_i p_i) \frac{r\phi}{A \sin(\alpha)} \quad (6.9)$$

where μ is the coefficient of friction between the layers, p is the interface pressure and r , ϕ and α are as previously defined. The stress to be considered in the life prediction of the composite helical tendons is then the sum of the stress produced by the pressure and tensile loading and the maximal additional stress due to pipe bending.

6.2 Implementation of Loading History into the Life Prediction Code

The next step in the life prediction process is to develop a code which incorporates the pipe loading history data into the remaining strength estimation scheme described in Chapter 5. An analysis of the flexible pipe in its service environment must first be conducted. Several papers that discuss this type of analysis have been published [28,30] and the pipe vendor should have the capability to provide this data. The inputs to this analysis include: wave scatter diagrams, the pipe stiffnesses and the geometry of the installation environment. Wave scatter diagrams supply wave data for the prospective service location. For a given time interval, this data is divided into sub-intervals by wave height. The wave frequency, horizontal offset and number of waves in each sub-interval are specified. An example of a simple wave scatter diagram for a 48 hour time interval with four sub-intervals is shown in Table 6.3 [25]. This diagram is used in the

hypothetical pipe analysis of Section 6.3. It should be noted that actual wave scatter diagrams are considerably more involved with numerous sub-intervals - each with its own wave height, frequency, direction and number of waves.

Table 6.3 Simplified wave scatter diagram for a 48 hour time period

Sub-interval	Wave Height (m)	Wave Period (sec)	Wave Direction	Number of Waves
1	2.0	9	In same	11150
2	4.0	9	direction	5363
3	6.0	9	for all	1009
4	8.0	9	cases	195

From a wave scatter diagram it is possible to calculate the variation in curvature and tension experienced by the flexible pipe during each sub-interval. This tension and curvature data along with the operating pressure of the pipe are then considered in the flexible pipe stress analysis of Section 6.1 to determine the maximum and minimum expected stresses in the composite helical armor for each sub-interval.

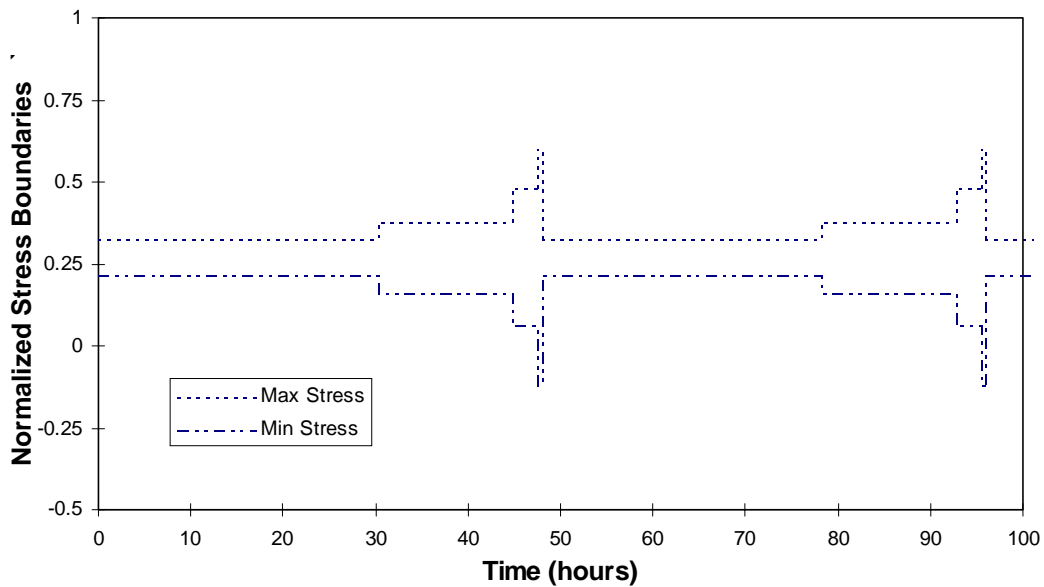


Figure 6.4 Maximum and minimum stress boundaries for a hypothetical pipe loading due to the wave scatter diagram in Table 6.3

We now have an estimation for the loading that the composite armor will encounter over time. Figure 6.4 shows an example of how the maximum and minimum stress boundaries may vary with time for the simplified wave scatter diagram of Table 6.3. This data is then used in an iterative code that reduces the remaining strength of the material for each time interval segment. We chose to approximate the cyclic loading experienced by the armor with a square wave form which alternates between the maximum and minimum stress at a frequency given by the wave scatter diagram. This decision simplifies the solution and should produce a conservative result. A diagram of this square wave loading is shown in Figure 6.5.

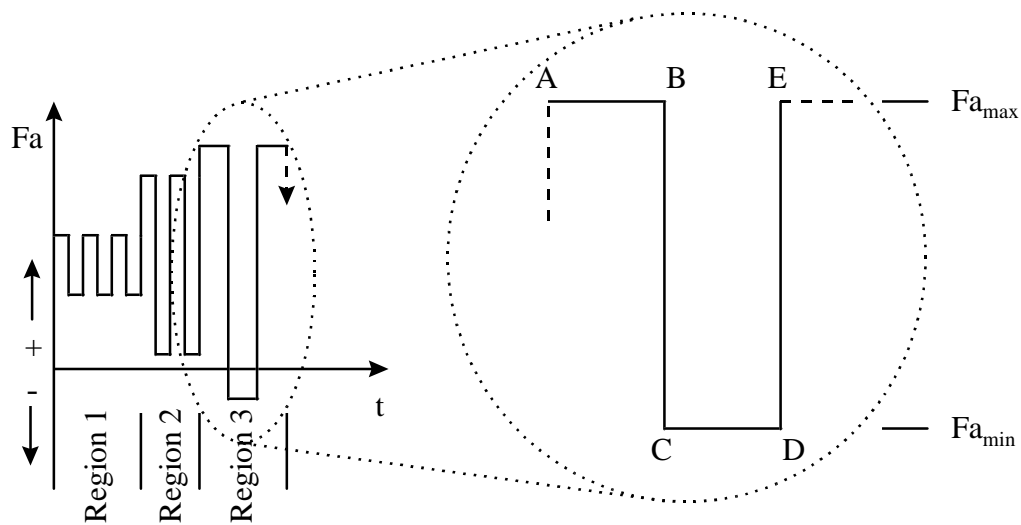


Figure 6.5 Approximated helical armor stress with respect to time

In the following discussion all references are made to Figure 6.5. In order to efficiently generate life estimations and still maintain accuracy, the cyclic loading was analyzed with different methods depending on the values of the applied stresses. If the R-

Ratio $\left(\frac{Fa_{\min}}{Fa_{\max}} \right)$ is greater than 0.3 and the stress never becomes compressive (e.g. Region

1) a characteristic time defined by Equation (5.4) is used in the evolution integral,

Equation (5.7), to compute the remaining strength after each time interval. In the evaluation of the evolution integral we will assume that the maximum normalized applied stress, F_a , remains constant over the given time interval. This additional assumption simplifies the remaining strength calculation and still maintains accuracy.

If on the other hand the R-Ratio is less than 0.3 and/or the stress drops below zero, a more complex strength reduction procedure must be employed. We found that, for R-Ratios less than 0.3 (e.g. Region 2), the rupture and fatigue combination scheme described above and in Section 5.1 will produce unconservative results. Also, for wave patterns which contain negative stresses (e.g. Region 3) this technique is not applicable at all since negative R-ratio values can not be used in Equation (5.4). As a result, the following concept was devised to reduce the strength over each cycle. On the interval between A and B the strength is reduced for a constant applied tensile rupture loading of $F_{a_{max}}$ for a duration equal to one half of the period. From B to C the reduction is due to one half cycle of fatigue. If $F_{a_{min}}$ is positive from C to D the strength will be reduced in the same a fashion as from A to B. However, if $F_{a_{min}}$ is compressive, the strength will be reduced for a constant applied bend-compression loading for a duration of one half period. The strength is then reduced again for one half cycle of fatigue for the interval D to E.

It is obvious that the second technique, outlined above, is considerably more involved since the strength must be reduced four times for a single wave cycle, whereas the first technique calculates the reduced strength for one entire time interval (which may consist of a plethora of wave cycles). Several test cases were run to study the use of the R-Ratio concept in comparison to the second technique and found that the loss in

accuracy due to the use of the R-Ratio scheme under the specified conditions was minimal. This conclusion allows life predictions to be calculated much more efficiently, especially considering that the material life is in the range of 1 to 20 years with an average wave period of approximately 9 seconds.

The Fortran code constructed to accomplish this iterative task is displayed in Appendix B. The next section describes the application of the above technique to a flexible pipe in a hypothetical environment.

6.3 Parameter analysis of a hypothetical flexible pipe

This section explains the life prediction of a hypothetical pipe in which several parameters are varied. Certain key factors are highlighted in this analysis which must be taken into account when designing a flexible pipe with composite helical armor. The parameters to be investigated are: the applied tensile load, the internal pipe pressure and the coefficient of friction between the composite armor and the adjacent layers.

6.3.1 Pipe description and loading

The flexible pipe under consideration has a six-inch internal diameter with two sets of contra-wound armor layers. Each set contains four helical layers of the composite tape described in Section 3.1 at a wrap angle of 25° with respect to the pipe axis. The calculated burst pressure for this pipe is 11,100 psi and the calculated failure tension is 1490 kips. The parameters for each load case and the applied normalized stresses and wave frequency for each sub-interval are shown in Table 6.4.

Table 6.4 Normalized armor stress, wave period and time interval length for each load case

Load Case	Sub-interval reference	Length of time interval (hours)	Max. Stress	Min. Stress	Wave Period (sec)
1.1 T = 400 kips P = 5000 psi, $\mu=0.1$					
	1	30.24	0.410	0.310	9
	2	14.52	0.465	0.255	9
	3	2.76	0.560	0.150	9
	4	0.480	0.700	0.010	9
1.2 T = 400 kips P = 5000 psi, $\mu=0.2$					
	1	30.24	0.414	0.307	9
	2	14.52	0.468	0.253	9
	3	2.76	0.574	0.147	9
	4	0.48	0.717	0.004	9
2.1 T = 400 kips P = 0 psi, $\mu=0.1$					
	1	30.24	0.322	0.215	9
	2	14.52	0.375	0.162	9
	3	2.76	0.480	0.060	9
	4	0.48	0.600	-0.120	9
2.2 T = 400 kips P = 0 psi, $\mu=0.2$					
	1	30.24	0.322	0.215	9
	2	14.52	0.376	0.161	9
	3	2.76	0.482	0.055	9
	4	0.48	0.622	-0.170	9
3.1 T = 200 kips P = 0 psi, $\mu=0.1$					
	1	30.24	0.188	0.080	9
	2	14.52	0.239	0.030	9
	3	2.76	0.330	-0.130	9
	4	0.48	0.402	-0.268	9
3.2 T = 200 kips P = 0 psi, $\mu=0.2$					
	1	30.24	0.188	0.080	9
	2	14.52	0.241	0.027	9
	3	2.76	0.345	-0.153	9
	4	0.48	0.468	-0.400	9

The four sub-intervals represent a 48 hour time span within a hypothetical pipe service history. The code described in Section 6.2 cycles through these four intervals repetitively and calculates the remaining strength at the conclusion of each interval. When the remaining strength drops below the applied stress, failure is declared and the life of the composite armor is defined as the time at which this occurs.

6.3.2 Conclusions drawn from the hypothetical pipe analysis

Figure 6.6 displays the remaining strength as a function of time for the six load cases described by Table 6.4. We can draw the following conclusions from this hypothetical pipe analysis.

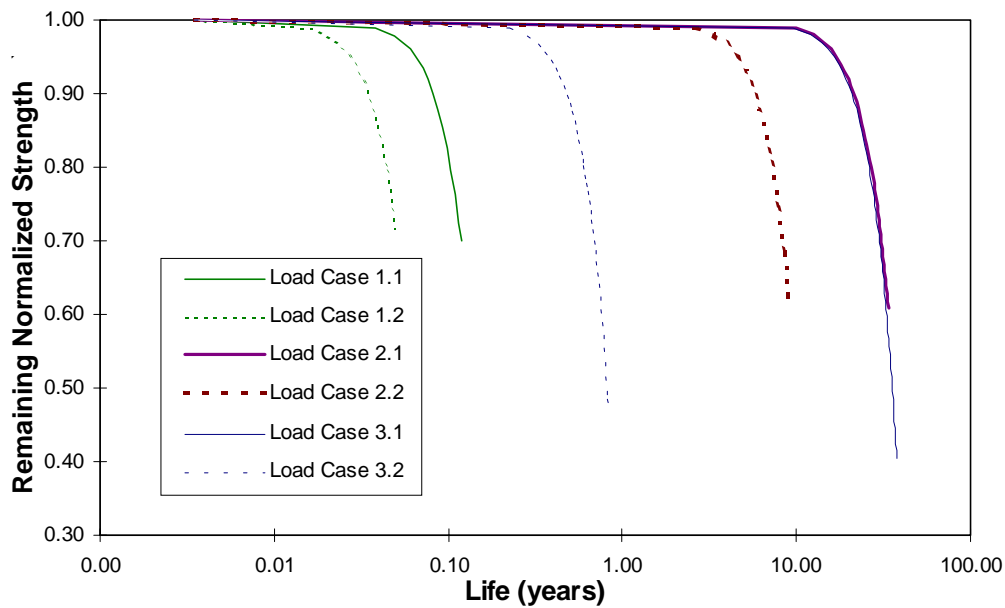


Figure 6.6 Remaining strength vs. time for composite armor

- As should be expected, the shortest pipe life occurs for the 1.x load cases since the applied stress is higher in comparison to the other cases. The primary damage

mechanism for the 1.x load cases is tensile rupture during sub-interval 4 even though this loading is only applied 1.0% of the time. From this observation we can conclude that “spikes” in the loading history, especially those with a normalized stress above 0.70, will substantially reduce the life of the composite.

- Load Cases 3.x demonstrates a different source for the primary strength reduction mechanism. Table 6.4 shows that the maximum stresses for load cases 3.1 and 3.2 are not substantially different, however the magnitude of the minimum stress in 3.2 is considerably larger than in 3.1. For this case compression rupture is the driver of the strength reduction. The difference in the lives between the two load cases is quite dramatic - the life of 3.2 is a factor of 30 less than the life of 3.1. This material is especially sensitive to compressive stresses with a magnitude greater than 35% of the compressive strength.
- The coefficient of friction between the layers plays a significant roll in reducing the life between all of the x.1 and x.2 load cases. We currently do not have coefficient of friction data for this material and its adjacent layers but, as can be seen, this is a factor that must be taken into account.

7. Conclusions and Future Work

- A service life model for a composite armor tendon within a flexible pipe in an offshore environment has been developed. The model is based on an iterative strength reduction scheme which considers the environmental conditions and variable cyclic loading characteristics of the expected service application.
- Comparison of elevated temperature experimental data with the life prediction results verified the model's effectiveness for the material under study.
- Prediction of elevated temperature tensile rupture behavior from bend-compression rupture data was accomplished via an analytical micromechanics model. This technique allows for a simplified and accelerated characterization of the material and may be applicable to other material systems.
- The analysis of a flexible pipe in a hypothetical environment led to the following conclusions: tensile rupture mechanisms are most significant for stresses above 70% ultimate tensile strength whereas compression rupture becomes detrimental at stress magnitudes above 35% ultimate compressive strength, the coefficient of friction between the composite armor and adjacent layers is an important factor and must be taken into account in the life prediction model.

7.1 Future Work

- Apply the life prediction model to an actual flexible pipe and its expected service environment.
- Experimentally determine the coefficient of friction between the composite armor and the adjacent layers and then include it in the analysis.

- With the correct coefficient of friction it will be possible to determine the slip-initiation pipe radius of curvature. It may then be possible to draw conclusions regarding fretting fatigue of the composite armor based on the number of slips that the armor experiences over time.
- Model the applied stress wave form with a more realistic sine wave form instead of the square wave pattern used in Section 6.2.
- Obtain experimental data for the behavior of the material at lower operating temperatures and in service conditions including: seawater, H₂S, and CO₂.
- Apply the tensile rupture prediction technique of Chapter 4 at different temperatures and to other material systems to check its generality.

8. References

1. Case, S.W., Xu, Y.L. and Reifsnider, K.L., *MRLife9TM A strength and Life Prediction Code for Laminated Composite Materials*, Materials Response Group, Virginia Tech, (1996).
2. Wimolkiatisak, A.S. and Bell, J.P., "Interfacial Shear Strength and Failure Modes of Interphase-modified Graphite-epoxy Composites," *Polym. Compos.*, v. 10 (3), (1989), pp. 162-172.
3. Ma, C.M., "Rheological, Thermal and Morphological Properties of High Performance Engineering Thermoplastic Resins and Composites," *Proc. Natl. Sci. Counc.*, v. 14 (4), (1990), pp. 245-258.
4. Schwartz, S.S. and Goodman, S.H., *Plastics Materials and Processes*, VanNostrand Reinhold Co., (1982), pp. 281-283, 420,474.
5. Brydson, J.A., *Plastics Materials*, Butterworths, (1989), 555-556.
6. Harper, C.A., *Handbook of Plastics and Elastomers*, McGraw-Hill Book Co., (1975), pp. 3-30, 3-45, 3-47.
7. Yau, S-S., Rhodes, V.H., Soules, D.A. and Cheng, P.J., "Characterization of Powder Coated Thermoplastic Composite," *23rd International SAMPE Technical Conference*, Kiamesha Lake, NY, (1991), pp. 1161-1168.
8. Myers, F.A., "Stress-State Effects on the Viscoelastic Response of Polyphenylene Sulfide (PPS) Based Thermoplastic Composites," *Advances in Thermoplastic Matrix Composite Materials, ASTM STP 1044*, (1989), pp. 154-182.

9. Lou, A.Y. and Murtha, T.P., "Environmental effects on glass fiber reinforced PPS," *J. Mat. Egr.*, v.10 (2), (1988), pp. 109-116.
10. Ma, C-C.M., Lee, C-L., Chang, M-J. and Tai, N-H, "Effect of Physical Aging of the Toughness of Carbon Fiber-Reinforced Poly(ether etherketone and Poly(phenylene sulfide) Composites. I," *Polym. Comp.*, v. 13 (6), (1992), pp.441-447.
11. Ma, C-C.M., Lee, C-L., Shen, H-S. and Ong, C-L., "Physical Aging of Carbon Fiber-Reinforced Polyether etherketone and Polyphenylene sulfide Composites (I)," *International SAMPE Symposium and Exhibition* , 35th, Anaheim, CA, (1990), pp. 1155-1166.
12. Kelly, A. and Nicholson, R.B. (eds.) *Strengthening Methods in Crystals*, Elsevier Pub. London, (1971).
13. Batdorf, S.B., "Unidirectionally Reinforced Composites - I," *J. Rein. Plastics and Comp.*, v. 1 (1982), pp. 153-164.
14. Gao, Z. and Reifsnider, K.L., "Micromechanics of Tensile Strength in Composite Systems," *Composite Materials; Fatigue and Fracture, Fourth Volume, ASTM STP 1156*, (1993), pp. 453-470.
15. Reifsnider, K.L., Iyengar, N., Case, S. and Xu, Y.L., "Damage tolerance and durability of fibrous material systems: A micro-kinetic approach," *Durability analysis of structural composite systems*, (1996), pp. 123-144.
16. Curtin, W.A., "Theory of Mechanical Properties of Ceramic-Matrix Composites," *J. Am. Ceram. Soc.*, v.74 (1991), pp. 2837-2845.
17. Tsai, S.W., and Hahn, T.H., *Introduction to Composite Materials*, Technomic Publishing Co. Inc., Lancaster, (1980), pp. 337-419.

18. Fleck, N.A. and Budiansky, B., "Compressive Failure of Fiber Composites due to Microbuckling," *IUTAM Symposium*, Troy, NY, (1990), pp. 235-273.
19. Reifsnider, K.L., "Use of Mechanistic Life Prediction Methods for the Design of Damage-Tolerant Composite Material Systems," *Advances in Fatigue Lifetime Predictive Techniques: Second Volume, ASTM STP 1211*, (1993), pp. 3-18.
20. Reifsnider, K.L., Case, S. and Iyengar, N., "Recent Advances in Composite Damage Mechanics," *European Space Agency*, Noordijk, Holland, 1996, in press.
21. Argon, A.S. and Bailey, D.G., "Failure in Laminates in Tension Under Increasing Stress, Constant Stress, and Cyclic Stress," *J. Mat. Sci.*, v. 9,(1974), 201-211.
22. Kliman, V., Fuleky, P. and Jelemenska, J., "Residual Operating Fatigue Lifetime - Estimation of Distribution Function," *Advances in Fatigue Lifetime Predictive Techniques: 3rd Volume, ASTM STP 1292*, (1996), pp. 305-327.
23. Shah, A.R., Murthy, P.L.N. and Chamis, C.C., "Effect of Cyclic Thermo-mechanical Load of Fatigue Reliability in Polymer Matrix Composites," *Proceedings of the 36th AIAA/ASME/ASCE/AHS/ASC Structures, Structural Dynamics, and Materials Conference*, New Orleans, LA, v. 3, (1995), pp. 1670-1683.
24. Jacobs, O., Freidrich, K., and Schulte, K., "Fretting Fatigue of Continuous Carbon Fiber Reinforced Polymer Composites," *Wear*, v. 145 (1), (1991), pp. 167-188.
25. Claydon, P., Cook, G., Brown, P.A. and Chandwani, R., "A Theoretical Approach to Prediction of Service Life of Unbonded Flexible Pipes under Dynamic Loading Conditions," *Marine Structures*, v. 5, (1992), pp. 399-429.

26. Saevik, S., and Berge, S., "Correlation between Theoretical Predictions and Testing of Two- 4-inch Flexible Pipes," *Energy-Sources Technology Conference and Exhibition*, Houston, TX, ASME Petroleum Div., PD v. 51, (1993), pp. 63-78.
27. Neffgen, J.M., "LAMS - Through Life Management for Flexible Pipe Systems," *Energy-Sources Technology Conference and Exhibition*, Houston, TX, ASME Petroleum Div., PD v. 51, (1993), pp. 5-11.
28. Ismail, N., Nielsen, R. and Kanarellis, M., "Design Considerations for Selection of Flexible Riser Configuration," *Energy-Sources Technology Conference and Exhibition*, Houston, TX, ASME Petroleum Div., PD v. 42, (1992), pp. 45-57.
29. Kalman, M.D., Belcher, J.R. and Plaia, J.R., "Advanced Materials for Flexible Pipe Construction," *Energy-Sources Technology Conference and Exhibition*, Houston, TX, ASME Petroleum Div., PD v. 68, (1995), pp. 155-167.
30. Robinson, J., Litzelfelner, J. and Dubea, C., "Flexible Pipe: QA/QC Requirements and Improved Installation Techniques," *Energy-Sources Technology Conference and Exhibition*, Houston, TX, ASME Petroleum Div., PD v. 42, (1992), pp. 39-44.
31. Timoshenko, S. P. and Gere, J. M. *Theory of Elastic Stability*, Second Ed., McGraw-Hill, New York, (1961).
32. Fukuda H., Kato H., Uesugi, H., "A Modified Procedure to Measure Bending Strength and Modulus of Advanced Composites by Means of Compression Bending," *Journal of Composite Materials*, v. 29 (2), (1995).
33. Fukuda, H., "A New Bending Test Method of Advanced Composites," *Experimental Mechanics*, v. 29 (4), (1989), pp. 330-335.

34. Mahieux, C.A., Stress Rupture of Unidirectional Polymer Matrix Composites in Bending at Elevated Temperatures, M.S. Thesis, Virginia Tech, (1996).
35. Personal Communication, Hood, D., William and Mary, 8-9-96.
36. Kachanov, L. M., *Introduction to continuum damage mechanics*. Martinus Nijhoff Publishers, Boston. (1986).
37. Personal Communication, Case, S., Virginia Tech, 3-5-97.

9. Appendix A - Hypothetical Unbonded Flexible Pipe Analysis

This worksheet was constructed with Mathcad 6.0 to calculate the stresses in each layer of a flexible pipe. The worksheet has been documented and should be self-explanatory for those with a basic working knowledge of Mathcad.

Loading (psi, lbf) - for Load Case 1.2; Sub-interval 4; Radius of curvature: $R=900$

$$P := 5000 \quad P = 5 \cdot 10^3 \quad \text{MaxP} := 11.1 \cdot 10^3$$

$$F := 400000 + \pi \cdot IR^2 \cdot P \quad F = 5.414 \cdot 10^5 \quad \text{MaxF} := 1.49 \cdot 10^6$$

Material Properties

	Steel	Nylon	Composite
Modulus	$E_s := 28.5 \cdot 10^6$	$E_n := .11 \cdot 10^6$	$E_c := 14 \cdot 10^6$
Shear Modulus	$G_s := 10.9 \cdot 10^6$	$G_n := .0377 \cdot 10^6$	$G_c := .25 \cdot E_c$
Poisson's Ratio	$\nu_s := .3$	$\nu_n := .45$	$\nu_c := .1$
Tensile Strength	$\sigma_{ults} := 85 \cdot 10^3$	$\sigma_{ultn} := 12 \cdot 10^3$	$\sigma_{ultc} := 185 \cdot 10^3$
Compressive Strength	$\sigma_{ultscr} := -85 \cdot 10^3$	$\sigma_{ultnrcr} := -12 \cdot 10^3$	$\sigma_{ultccr} := -93 \cdot 10^3$

Geometry

Inner Radius $IR=3$
 Number of layers $N := 14$
 Minimum bend radius for pipe (used to determine spacing between wraps) $\text{MinRad} := 75$

	Width	Thickness	Wrap Angle
Carcass	$w_C := .1$	$t_C := .4$	$\alpha_C := 87 \cdot \text{deg}$
Fluid Barrier		$t_{FB} := .5$	
Flexlok	$w_F := .6$	$t_F := .6$	$\alpha_F := -87 \cdot \text{deg}$
Sheath1	$w_S := 100$	$t_{S1} := .2$	
Armor	$w_A := .5$	$t_A := .04$	$\alpha_A := 25 \cdot \text{deg}$
Sheath2		$t_{S2} := .5$	

$w_i :=$	$t_i :=$	$\alpha_i :=$	$E_i :=$	$G_i :=$	$\nu_i :=$	$\sigma_{ult_i} :=$	$\sigma_{ultcr_i} :=$
wC	tC	α_C	E_s	G_s	ν_s	σ_{ults}	σ_{ultscr}
wS	tFB	0.1	E_n	G_n	ν_n	σ_{ultn}	$\sigma_{ultnrcr}$
wF	tF	α_F	E_s	G_s	ν_s	σ_{ults}	σ_{ultscr}
wS	tS1	0.1	E_n	G_n	ν_n	σ_{ultn}	$\sigma_{ultnrcr}$
wA	tA	α_A	E_c	G_c	ν_c	σ_{ultc}	σ_{ultccr}
wA	tA	α_A	E_c	G_c	ν_c	σ_{ultc}	σ_{ultccr}
wA	tA	α_A	E_c	G_c	ν_c	σ_{ultc}	σ_{ultccr}
wA	tA	α_A	E_c	G_c	ν_c	σ_{ultc}	σ_{ultccr}
wA	tA	α_A	E_c	G_c	ν_c	σ_{ultc}	σ_{ultccr}
wS	tS1	0.1	E_n	G_n	ν_n	σ_{ultn}	$\sigma_{ultnrcr}$
wA	tA	$-\alpha_A$	E_c	G_c	ν_c	σ_{ultc}	σ_{ultccr}
wA	tA	$-\alpha_A$	E_c	G_c	ν_c	σ_{ultc}	σ_{ultccr}
wA	tA	$-\alpha_A$	E_c	G_c	ν_c	σ_{ultc}	σ_{ultccr}
wA	tA	$-\alpha_A$	E_c	G_c	ν_c	σ_{ultc}	σ_{ultccr}
wS	tS2	0.1	E_n	G_n	ν_n	σ_{ultn}	$\sigma_{ultnrcr}$

Mean Radii

$$r_1 := IR + .5 \cdot t_1 \quad i := 2..14 \quad r_i := r_{i-1} + .5 \cdot t_{i-1} + .5 \cdot t_i$$

r_i
3.65
4.2
4.6
4.72
4.76
4.8
4.84
4.96
5.08
5.12
5.16
5.2
5.47

Layer Cross-sectional Properties $i := 1..14$

Area $A_i := \text{if}(\alpha_i = 0.1, 2 \cdot \pi \cdot r_i \cdot t_i, w_i \cdot t_i)$

Moment of Inertia $I_i := \frac{w_i \cdot (t_i)^3}{12}$

Polar Moment of Inertia $J_i := \frac{w_i \cdot t_i \cdot [(t_i)^2 + (w_i)^2]}{12}$

Number of wraps

$$\frac{w + g}{g} = \frac{\text{MinRad}}{r} \quad g_1 := \frac{-w_i \cdot r_i}{r_i - \text{MinRad}} \quad g_1 := .5 \quad \text{pitch}_1 := w_i + g_1$$

$$jt_1 := \frac{w_i}{\text{pitch}_1} \quad n_1 := \text{floor}\left(\frac{1}{w_i} \cdot 2 \cdot \pi \cdot r_i \cdot jt_1 \cdot \cos(\alpha_i)\right)$$

n_i
1
0
2
0
50
50
51
51
0
53
54
54
55
0

Equilibrium Equations in Polymer Layers

$$\Delta P_{\text{cyl}_1} = P_{\text{rcyl}_1} \cdot \Delta r + P_{\text{l cyl}_1} \cdot \Delta l$$

$$P_{\text{rcyl}_1} := \frac{E_i \cdot t_i}{(r_i)^2 \cdot [1 - (\nu_i)^2]}$$

$$P_{\text{l cyl}_1} := \frac{\nu_i \cdot E_i \cdot t_i}{r_i \cdot [1 - (\nu_i)^2]}$$

$$F_{a_{\text{cyl}_1}} = F_{\text{rcyl}_1} \cdot \Delta r + F_{\text{l cyl}_1} \cdot \Delta l$$

$$F_{\text{rcyl}_1} := \frac{\nu_i \cdot 2 \cdot \pi \cdot E_i \cdot t_i}{1 - (\nu_i)^2}$$

$$F_{\text{l cyl}_1} := \frac{2 \cdot \pi \cdot E_i \cdot r_i \cdot t_i}{[1 - (\nu_i)^2]}$$

Equilibrium Equations in Helical Layers

$$\Delta P_{\text{hel}_1} = P_{\text{r hel}_1} \cdot \Delta r + P_{\text{l hel}_1} \cdot \Delta l$$

$$P_{\text{r hel}_1} := \frac{n_i \cdot |\tan(\alpha_i)|}{2 \cdot \pi \cdot r_i} \cdot \left[\left[\frac{(|\sin(\alpha_i)|)^3 \cdot \cos(\alpha_i)^2 \cdot \cos(2 \cdot \alpha_i)}{(r_i)^4} \cdot E_i \cdot I_i \right] - \left[\frac{2 \cdot \cos(\alpha_i)^4 \cdot (|\sin(\alpha_i)|)^3}{(r_i)^4} \cdot G_i \cdot J_i \right] + \left[\frac{(|\sin(\alpha_i)|)^3}{(r_i)^2} \cdot E_i \cdot A_i \right] \right]$$

$$P_{\text{l hel}_1} := \frac{n_i \cdot |\tan(\alpha_i)|}{2 \cdot \pi \cdot r_i} \cdot \left[\left[\frac{-2 \cdot (|\sin(\alpha_i)|)^3 \cdot \cos(\alpha_i)^4}{(r_i)^3} \cdot E_i \cdot I_i \right] - \left[\frac{(|\sin(\alpha_i)|)^3 \cdot \cos(\alpha_i)^2 \cdot (\sin(\alpha_i)^2 - \cos(\alpha_i)^2)}{(r_i)^3} \cdot G_i \cdot J_i \right] \dots \right. \\ \left. + \left[\frac{|\sin(\alpha_i)| \cdot \cos(\alpha_i)^2}{r_i} \cdot E_i \cdot A_i \right] \right]$$

$$F_{a_{\text{hel}_1}} = F_{\text{r hel}_1} \cdot \Delta r + F_{\text{l hel}_1} \cdot \Delta l$$

$$F_{\text{r hel}_1} := n_i \cdot \left[\frac{\sin(\alpha_i)^4 \cdot \cos(\alpha_i) \cdot \cos(2 \cdot \alpha_i)}{(r_i)^3} \cdot E_i \cdot I_i + \frac{2 \cdot \sin(\alpha_i)^4 \cdot \cos(\alpha_i)^3}{(r_i)^3} \cdot G_i \cdot J_i + \frac{\sin(\alpha_i)^2 \cdot \cos(\alpha_i)}{r_i} \cdot E_i \cdot A_i \right]$$

$$F_{\text{l hel}_1} := n_i \cdot \left[\frac{2 \cdot \sin(\alpha_i)^4 \cdot \cos(\alpha_i)^3}{(r_i)^2} \cdot E_i \cdot I_i + \frac{\sin(\alpha_i)^4 \cdot \cos(\alpha_i) \cdot (\sin(\alpha_i)^2 - \cos(\alpha_i)^2)}{(r_i)^2} \cdot G_i \cdot J_i + \cos(\alpha_i)^3 \cdot E_i \cdot A_i \right]$$

Define references to Cylindrical (cl) and Helical (hl) layers

j := 1..4
cl_j :=

2
4
9
14

k := 1..9
hl_k :=

3
5
6
7
8
10
11
12
13

Compatibility and Equilibrium of whole pipe give 2 equations which are solved for Δr and Δl

Δr := .01 Δl := 1

Given

$$P = \left[\sum_j P_{\text{cyl}}(\text{cl}_j) + \sum_k P_{\text{hel}}(\text{hl}_k) \right] \cdot \Delta r + \left[\sum_j P_{\text{cyl}}(\text{cl}_j) + \sum_k P_{\text{hel}}(\text{hl}_k) \right] \cdot \Delta l$$

$$F = \left[\sum_j F_{\text{cyl}}(\text{cl}_j) + \sum_k F_{\text{hel}}(\text{hl}_k) \right] \cdot \Delta r + \left[\sum_j F_{\text{cyl}}(\text{cl}_j) + \sum_k F_{\text{hel}}(\text{hl}_k) \right] \cdot \Delta l$$

$$\begin{pmatrix} \Delta r \\ \Delta l \end{pmatrix} := \text{Find}(\Delta r, \Delta l) \quad \begin{pmatrix} \Delta r \\ \Delta l \end{pmatrix} = \begin{pmatrix} 0.004866 \\ 0.005595 \end{pmatrix} \quad \begin{array}{l} \Leftarrow \text{radial displacement (constant through wall)} \\ \Leftarrow \text{axial strain of pipe} \end{array}$$

Change in Pressure through each layer (the carcass, $i=1$, is surrounded by fluid and thus does not contain pressure) $i := 2..N$

$$\Delta P_{cyl_i} := P_{rcyl_i} \cdot \Delta r + P_{l_{cyl_i}} \cdot \Delta l$$

$$\Delta P_{hel_i} := P_{r_{hel_i}} \cdot \Delta r + P_{l_{hel_i}} \cdot \Delta l$$

$$\Delta P_i := \text{if}(\alpha_i = 0.1, \Delta P_{cyl_i}, \Delta P_{hel_i})$$

$$\Delta P_i$$

72.762
$4.13 \cdot 10^3$
21.443
94.21
92.603
92.858
91.301
19.46
85.975
86.21
84.855
85.078
42.96

$$\sum_{i=2}^N \Delta P_i = 5 \cdot 10^3$$

Interface and Contact Pressures

$$P_{int_i} := P - \sum_{q=2}^i \Delta P_q$$

$$P_{int_i}$$

$4.927 \cdot 10^3$
796.953
775.51
681.3
588.696
495.838
404.537
385.078
299.103
212.893
128.038
42.96
$9.095 \cdot 10^{-13}$

$$P_{cnt_i} := P_{int_i} \cdot \frac{w_i}{w_i - g_i}$$

$$P_{cnt_i}$$

$5.193 \cdot 10^3$
847.211
829.725
730.35
631.491
532.23
434.512
414.426
322.536
229.725
138.253
46.418
$9.872 \cdot 10^{-13}$

Axial force supported by each layer

$$Fa_{cyl_i} := Fr_{cyl_i} \cdot \Delta r + Fl_{cyl_i} \cdot \Delta l$$

$$Fa_{hel_i} := Fr_{hel_i} \cdot \Delta r + Fl_{hel_i} \cdot \Delta l$$

$$Fa_i := \text{if}(\alpha_i = 0.1, Fa_{cyl_i}, Fa_{hel_i})$$

Fa_i
$9.798 \cdot 10^3$
$1.267 \cdot 10^3$
$4.84 \cdot 10^3$
$6.065 \cdot 10^4$
$6.063 \cdot 10^4$
$6.182 \cdot 10^4$
$6.18 \cdot 10^4$
$5.19 \cdot 10^3$
$6.411 \cdot 10^4$
$6.53 \cdot 10^4$
$6.528 \cdot 10^4$
$6.647 \cdot 10^4$
$1.421 \cdot 10^4$

$$\sum_{i=1}^N Fa_i = 5.414 \cdot 10^5 \quad F = 5.414 \cdot 10^5$$

Forces and stresses in helical layers

Coefficient of friction between layers $\mu_i := .2$

Stresses are greatest at $\phi := \frac{\pi}{2}$

$$fa_i := \frac{Fa_{hel_i}}{n_i}$$

$$p_i := \frac{2 \cdot \pi \cdot r_i \cdot \Delta P_{hel_i}}{n_i \cdot |\tan(\alpha_i)|}$$

$$fx_i := fa_i \cdot \cos(\alpha_i) + r_i \cdot p_i \cdot |\sin(\alpha_i)|$$

Bending stresses for pipe Radius of curvature (in): R = 900

Use ETB if layers not slipping

$$\sigma_{\text{addbend}1_i} := \frac{E_i \cdot r_i \cdot |\sin(\phi)|}{R} \cdot \cos(\alpha_i)^2$$

$\sigma_{\text{addbend}1_i}$
441.665
364.294
556.619
$6.031 \cdot 10^4$
$6.082 \cdot 10^4$
$6.133 \cdot 10^4$
$6.184 \cdot 10^4$
600.18
$6.491 \cdot 10^4$
$6.542 \cdot 10^4$
$6.593 \cdot 10^4$
$6.644 \cdot 10^4$
661.892

If slipping take into account friction due to contact pressures

$$\sigma_{\text{addbend}2_i} := \frac{(\mu_{i-1} \cdot \text{Pcnt}_{i-1} + \mu_i \cdot \text{Pcnt}_i) \cdot r_i \cdot \phi}{A_i \cdot |\sin(\alpha_i)|}$$

$\sigma_{\text{addbend}2_i}$
$5.202 \cdot 10^3$
$2.217 \cdot 10^4$
$4.199 \cdot 10^3$
$2.737 \cdot 10^5$
$2.409 \cdot 10^5$
$2.076 \cdot 10^5$
$1.739 \cdot 10^5$
$2.126 \cdot 10^3$
$1.391 \cdot 10^5$
$1.051 \cdot 10^5$
$7.057 \cdot 10^4$
$3.569 \cdot 10^4$
46.495

Maximum Stress and Normalized Stress in Layers

$$\sigma_{\max i} := \text{if} \left(\alpha_i = 0.1, \frac{F a_i}{A_i} + \sigma_{\text{addbend}1_i}, \frac{f x_i}{A_i} + \text{if} \left(\sigma_{\text{addbend}1_i} \leq \sigma_{\text{addbend}2_i}, \sigma_{\text{addbend}1_i}, \sigma_{\text{addbend}2_i} \right) \right)$$

$$\sigma_{\max N_i} := \frac{\sigma_{\max i}}{\sigma_{\text{ult}i}}$$

$\sigma_{\max i}$	$\sigma_{\max N_i}$
1.296 · 10 ³	0.108
3.373 · 10 ⁴	0.397
1.394 · 10 ³	0.116
1.272 · 10 ⁵	0.688
1.277 · 10 ⁵	0.69
1.282 · 10 ⁵	0.693
1.287 · 10 ⁵	0.696
1.433 · 10 ³	0.119
1.316 · 10 ⁵	0.712
1.321 · 10 ⁵	0.714
1.326 · 10 ⁵	0.717
1.024 · 10 ⁵	0.553
1.489 · 10 ³	0.124

Minimum Stress and Normalized Stress in Layers

$$\sigma_{\min i} := \text{if} \left(\alpha_i = 0.1, \frac{F a_i}{A_i} - \sigma_{\text{addbend}1_i}, \frac{f x_i}{A_i} - \text{if} \left(\sigma_{\text{addbend}1_i} \leq \sigma_{\text{addbend}2_i}, \sigma_{\text{addbend}1_i}, \sigma_{\text{addbend}2_i} \right) \right)$$

If the stress is negative normalize it by the compressive strength

$$\sigma_{\min N_i} := \text{if} \left[\sigma_{\min i} < 0, \frac{\sigma_{\min i}}{(\sigma_{\text{ultcr}i})}, \frac{\sigma_{\min i}}{(\sigma_{\text{ult}i})} \right]$$

$\sigma_{\min i}$	$\sigma_{\min N_i}$
412.8	0.034
3.3 · 10 ⁴	0.388
280.756	0.023
6.608 · 10 ³	0.036
6.075 · 10 ³	0.033
5.543 · 10 ³	0.03
5.011 · 10 ³	0.027
5.011 · 10 ³	0.019
232.429	0.01
1.826 · 10 ³	0.007
1.296 · 10 ³	0.004
766.429	0.167
3.099 · 10 ⁴	0.014
165.039	

10. Appendix B - Iterative Remaining Strength Calculation Program

This program is based on the MRLife code developed by the Materials Response Group at Virginia Tech. Only the capabilities of MRLife necessary for this application are included in order to streamline the code. The modifications to MRLife as discussed in Sections 5.1 and 6.2 have been implemented. The documented code below was written in Fortran 90 using Microsoft Developer.

```
! PROGRAM MRFLIPE4
!
! Computes remaining strength of composite armor in a flexible pipe for
! a square wave loading which alternates between the max and min
! normalized stresses at a given frequency. Varying amplitudes over
! different time periods are allowed.
! If the R-Ratio is greater than 0.3 and the applied stress never
! becomes negative, a scheme which combines fatigue and rupture
! effects via the R-Ratio is used to reduce the strength. This
! technique runs considerably faster than and produces comparable
! results, for the conditions mentioned, to the more complicated model
! described next.
! If the previously mentioned conditions are not met the loading is
! modeled as follows. Tensile loads are modeled with tensile rupture
! curve, while compressive loads use the bend rupture curve. Fatigue
! is taken into account by reducing the strength for 1/2 cycle of
! fatigue after each segment of rupture.
!
! Inputs: For each time interval (read in through a data file - one
! line for each interval)
!   delt - Length of time interval
!   Famax0 - Max stress over time interval
!   Famin0 - Min stress over time interval (negative if compressive)
!   j - j value used in evolution integral
!   f - wave frequency
!
!
! IMPLICIT REAL*8 (A-H,J,N-Z)
!
! Tensile rupture curve constants
! At = 2467.132
! nt = 36.69569
!
! Bend rupture curve constants
! Ab = 16.17908484
! nb = 9.588118887
!
! S-N curve constants
! An = 0.920666
! Bn = -.018774
!
! Initialize variables
! Famax = 0.5
```

```

Famin = 0.5
Fr_p = 1.0
t_elpsd = 0.0
netdelFr = 0.0
prevdel = 1.0

! Setup output file
OPEN(139, FILE='otws1_2.dat')
WRITE(139,15) 't_elpsd (yr)', 'Famax0', 'Famin0', 'Fr', 'tauht_max',
&
'tauht_min', 't0max', 't0min'
15 FORMAT (A,T20,A,T35,A,T50,A,T65,A,T80,A,T95,A,T110,A)

40 OPEN(39, FILE='inws1_2.dat')

! Main loop - iterates time interval
DO WHILE ((ABS(Famax0) .LE. Fr_p) .AND. (ABS(Famin0) .LE. Fr_p))

! Read loading for current time interval
READ(39,*,END=133) delt,Famax0,Famin0,j,f

R = Famin0/Famax0

! Check for negative stress values and R-Ratio < 0.3
IF (((Famax0 .GT. 0.) .AND. (Famin0 .GT. 0.)) .AND.
& (R .GE. 0.3)) THEN

! R-Ratio scheme for strength reduction
tr = (1/((nt+1)*At*Famax0**nt))*3600
tf = (10**((Famax0-An)/Bn))/f
tauht = 1/(R/tr+(1-R)/tf)
t0 = (((1-Fr_p)/(1-Famax0))*(1/j))*tauht
delFr = -(1-Famax0)*(((t0+delt)/tauht)**j - (t0/tauht)**j)
netdelFr = netdelFr + delFr
Fr_p = 1. + netdelFr
t_elpsd = t_elpsd + delt

ELSE

! Single wave integration scheme for strength reduction
numsub = NINT(delt*f)
per = 1./f

IF (Famax0 .GT. 0.) THEN
tauht_max = (1/((nt+1.)*At*Famax0**nt))*3600.
ELSE
tauht_max = (1/((nb+1.)*Ab*(-Famax0)**nb))*3600.
END IF
Famax = ABS(Famax0)
N_f1 = 10.**((Famax-An)/Bn)

IF (Famin0 .GT. 0.) THEN
tauht_min = (1/((nt+1.)*At*Famin0**nt))*3600.
ELSE
tauht_min = (1/((nb+1.)*Ab*(-Famin0)**nb))*3600.
END IF
Famin = ABS(Famin0)
N_f2 = 10.**((Famin-An)/Bn)

```

```

! Secondary loop - Calculates Remaining strength after each wave cycle
DO 200 k = 1,numsub

    IF ((Famax .GT. Fr_p) .OR. (Famin .GT. Fr_p)) EXIT

! Max stress section
    t0max = (((1.-Fr_p)/(1.-Famax))**(1./j))*tauht_max
    delFrmax = -(1.-Famax)*(((t0max+per/2.)/tauht_max)
    &          **j - (t0max/tauht_max)**j)
    netdelFr = netdelFr + delFrmax
    Fr_p = 1. + netdelFr

! 1/2 cycle of fatigue
    t0f1 = (((1.-Fr_p)/(1.-Famax))**(1./j))*N_f1
    vall = ((t0f1+.5)/N_f1)**j
    delFrfl = -(1.-Famax)*(((t0f1+.5)/N_f1)
    &          **j - (t0f1/N_f1)**j)
    netdelFr = netdelFr + delFrfl
    Fr_p = 1. + netdelFr

! Min stress section
    t0min = (((1.-Fr_p)/(1.-Famin))**(1./j))*tauht_min
    delFrmin = -(1.-Famin)*(((t0min+per/2.)/tauht_min)
    &          **j - (t0min/tauht_min)**j)
    netdelFr = netdelFr + delFrmin
    Fr_p = 1. + netdelFr

! 1/2 cycle of fatigue
    t0f2 = (((1.-Fr_p)/(1.-Famin))**(1./j))*N_f2
    delFrff2 = -(1.-Famin)*(((t0f2+.5)/N_f2)
    &          **j - (t0f2/N_f2)**j)
    netdelFr = netdelFr + delFrff2
    Fr_p = 1. + netdelFr

    numsubcomp = k*1.0

! End secondary loop
200 CONTINUE

    t_elpsd = t_elpsd + numsubcomp/f

    END IF

! Write remaining strength info after time interval to file
! Only writes to file after reduction by an additional 0.01
    IF ((netdelFr-prevdel) .LT. -0.01) THEN
        prevdel=netdelFr
        WRITE(*,*) 'Fa = ',Famax0,' Fr = ',Fr_p
        WRITE(139,20) t_elpsd/3600./24./365.,Famax0,Famin0,Fr_p,
        &          tauht_max,tauht_min,t0max,t0min
    20 FORMAT (G13.4,7(TR2,E13.5))
    END IF

    WRITE(*,*) 'Fr = ', Fr_p

! End primary loop
    END DO

```

```
! If the armor has not failed after the given sequence of time
! intervals, the program will repeatedly run through the sequence
! until failure.

133  IF ((ABS(Famax0) .LE. Fr_p) .AND. (ABS(Famin0) .LE. Fr_p)) THEN
      CLOSE(39)
      WRITE(*,*) 'Fr = ', Fr_p
      GOTO 40
    END IF

    CLOSE(39)
    CLOSE(139)

    END

! Adios!
```

11. Vita

James S. Loverich arrived on October 9, 1972 in Winner South Dakota. He spent most of his “growing-up” years in Flagstaff, Arizona building go-karts and launching rockets. After graduating from Flagstaff High School in 1991, he enrolled in Northern Arizona University. He graduated Summa Cum Laude in 1995 with a B.S. degree in Mechanical Engineering. In the fall of that year he entered the M.S. program in Engineering Science and Mechanics at Virginia Polytechnic Institute and State University. James enjoys racing mountain bikes and hopes to pursue a career in bicycle design.